

1 Manuscript published in Agricultural and Forest Meteorology.

2 DOI: 10.1016/j.agrformet.2023.109408.

3 Link to the published paper: <https://doi.org/10.1016/j.agrformet.2023.109408>

4 © 2023. This manuscript version is made available under the CC-BY-NC-ND 4.0 license

5 <https://creativecommons.org/licenses/by-nc-nd/4.0/>

6

7 **STEEP: a remotely-sensed energy balance model for evapotranspiration estimation in**
8 **seasonally dry tropical forests**

9 Ulisses A. Bezerra^{a*}, John Cunha^a, Fernanda Valente^b, Rodolfo L. B. Nóbrega^{c,d}, João M. Andrade^e, Magna
10 S. B. Moura^f, Anne Verhoef^g, Aldrin M. Perez-Marin^h, Carlos O. Galvão^a

11 ^aFederal University of Campina Grande, Centre for Natural Resources and Technology, Campina Grande, Brazil

12 ^bForest Research Centre (CEF), School of Agriculture, University of Lisbon, Tapada da Ajuda, 1349-017 Lisbon, Portugal

13 ^cUniversity of Bristol, School of Geographical Sciences, University Rd, Bristol, BS8 1SS, UK

14 ^dImperial College London, Georgina Mace Centre for the Living Planet, Department of Life Sciences, Silwood Park
15 Campus, Buckhurst Road, Ascot, SL5 7PY, UK

16 ^eFederal University of Pernambuco, Department of Civil and Environmental Engineering, Recife, Brazil

17 ^fEmpresa Brasileira de Pesquisa Agropecuária, Embrapa Semiárido, Petrolina, Brazil

18 ^gThe University of Reading, Department of Geography and Environmental Science, UK

19 ^hInstituto Nacional do Semiárido/Núcleo de Desertificação e Agroecologia, Campina Grande, Brazil

20 *Corresponding author: ulisses.alencar@estudante.ufcg.edu.br; ulisses.alencar17@gmail.com

21 **Highlights**

- 22 ● STEEP is a RS-based SEB model from a one-source bulk transfer equation for SDTF.
23 ● STEEP includes improved representations of phenology and soil moisture for SDTF.
24 ● STEEP is tested against eddy covariance data from the largest SDTF in South America.
25 ● STEEP exhibits satisfactory metrics and outperforms SEBAL, MOD16, and PMLv2.

26 **Abstract**

27 Improvement of evapotranspiration (ET) estimates using remote sensing (RS) products based on
28 multispectral and thermal sensors has been a breakthrough in hydrological research. In large-scale
29 applications, methods that use the approach of RS-based surface energy balance (SEB) models
30 often rely on oversimplifications. The use of these models for Seasonally Dry Tropical Forests
31 (SDTF) has been challenging due to incompatibilities between the assumptions underlying those

32 models and the specificities of this environment, such as the highly contrasting phenological phases
33 or ET being mainly controlled by soil–water availability. We developed a RS-based SEB model from
34 a one-source bulk transfer equation, called Seasonal Tropical Ecosystem Energy Partitioning
35 (STEEP). Our model uses the plant area index to represent the woody structure of the plants in
36 calculating the moment roughness length. We included the parameter kB^{-1} and its correction using
37 RS soil moisture in the calculation of the aerodynamic resistance for heat transfer.
38 Besides, λET caused by remaining water availability in endmembers pixels was quantified using the
39 Priestley-Taylor equation. We implemented the algorithm on Google Earth Engine, using freely
40 available data. To evaluate our model, we used eddy covariance data from four sites in the Caatinga,
41 the largest SDTF in South America, in the Brazilian semiarid region. Our results show that STEEP
42 increased the accuracy of ET estimates without requiring any additional climatological information.
43 This improvement is more pronounced during the dry season, which, in general, ET for these SDTF
44 is overestimated by traditional SEB models, such as the Surface Energy Balance Algorithms for Land
45 (SEBAL). The STEEP model had similar or superior behavior and performance statistics relative to
46 global ET products (MOD16 and PMLv2). This work contributes to an improved understanding of the
47 drivers and modulators of the energy and water balances at local and regional scales in SDTF.
48 Keywords: Sensible heat flux, Aerodynamic resistance for heat transfer, Surface energy balance,
49 Caatinga, Google Earth Engine

50

51 **1. Introduction**

52 Quantifying evapotranspiration (ET) is one of the largest research challenges in hydrology
53 because ET is driven by a complex combination of atmospheric, vegetation, edaphic, and terrain
54 characteristics (Wang et al., 2016; Bhattarai et al., 2017). The traditional techniques to quantify ET,
55 e.g. Bowen ratio or eddy covariance system (EC), are limited to areas up to ~ 10 km² (Allen et al.,
56 2011; Anapalli et al., 2016; Mcshane et al., 2017; Mallick et al., 2018; Chu et al., 2021). Over the
57 past decades, models based on satellite remote sensing (RS) data have been increasingly
58 developed and applied to estimate ET for multiple temporal and spatial scales (Anderson et al., 2011;
59 Chen and Liu, 2020). RS-based surface energy balance (SEB) models estimate ET in terms of
60 energy per unit area (e.g. W/m²), i.e. by latent heat flux, λET , where λ is the latent heat of vaporization

61 of water (Shuttleworth, 2012; Barraza et al., 2017; Trebs et al., 2021). SEB models obtain λET by
62 subtracting the soil heat (G) and sensible heat (H) fluxes from the net radiation (R_n). Estimates of R_n
63 obtained with RS data have been improving, and this flux can nowadays be estimated with
64 acceptable precision (Allen et al., 2011; Ferreira et al., 2020). The $G:R_n$ ratio can be predicted with
65 reasonable accuracy through the use of empirical relationships with soil, vegetation, and temperature
66 characteristics (Bastiaanssen, 1995; Murray and Verhoef, 2007; Allen et al., 2011; Danelichen et al.,
67 2014). Challenges in estimating λET as a residual of the energy balance are mostly associated with
68 the uncertainties in H (Gokmen et al., 2012; Paul et al., 2014; Mohan et al., 2020a, Mohan et al.,
69 2020b; Costa-Filho et al., 2021). The bulk heat transfer calculation that is used to compute H involves
70 variables related to the temperature gradient and to the aerodynamic resistance for heat transfer
71 (rah). If any of these variables are poorly estimated, the performance of SEB models will be reduced
72 (Verhoef et al., 1997a, b; Su et al., 2001; Gokmen et al., 2012; Costa-Filho et al., 2021; Liu et al.,
73 2021; Trebs et al., 2021).

74 The difference between the aerodynamic surface temperature and air temperature (dT)
75 drives H . However, the lack of techniques to measure the aerodynamic surface temperature required
76 strategies to use the radiometric land surface temperature (LST) as an alternative. Bastiaanssen et
77 al. (1998), when creating the Surface Energy Balance Algorithms for Land (SEBAL), proposed that
78 dT can be estimated with a linear relationship on LST. This requires identifying areas with contrasting
79 extreme conditions in terms of cover and humidity, e.g., dry bare and well-watered soil surfaces,
80 commonly known as hot/dry and cold/wet endmembers, respectively. The sensible heat transfer
81 equation in conjunction with the surface energy balance in hot/dry and cold/wet endmembers allows
82 one to obtain the coefficients of the linear relationship between dT and LST. Bastiaanssen et al.
83 (1998) proposed the selection of endmembers by assuming that H in the cold/wet endmember and
84 λET in the hot/dry endmember are zero. However, these assumptions are not necessarily valid
85 (Singh and Irmak, 2011; Singh et al., 2012). The cold/wet endmember refers to an area with a well-
86 irrigated crop surface having ground fully covered by vegetation, so it can be assumed that a non-
87 negligible amount of sensible heat can still be generated by such a surface. Similarly, for the hot/dry
88 endmember, an area dominated by bare soil, there may be a λET resulting from antecedent rainfall
89 events, hereafter referred to as remaining λET . Some studies have quantified H and λET in hot/dry

90 and cold/wet endmembers (Trezza, 2006; Allen et al., 2007; Singh and Irmak, 2011); they have
91 shown that this quantification produces a better approximation of daily ET.

92 Based on the Monin-Obukhov similarity theory, *rah* is defined as a function of the momentum
93 (*z0m*) and heat (*z0h*) roughness lengths. Theoretically, the sum of the zero plane displacement
94 height (*d0*) together with *z0h* defines the level of the effective source of sensible heat (Thom, 1972;
95 Chehbouni et al., 1996; Gokmen et al., 2012) and, therefore, *z0h* constitutes one of the most crucial
96 parameters for the accurate calculation of *H* (Verhoef et al., 1997a; Su et al., 2001). However, as
97 *z0h* cannot be measured directly, it is commonly calculated via the dimensionless parameter kB^{-1}
98 formulated to express the excess resistance of heat transfer compared to momentum transfer (Owen
99 and Thomson, 1963). In RS-based SEB models, oversimplifications are present in the calculation of
100 *rah*, e.g. different land use types are represented by the same values for *z0h* (Bastiaanssen et al.,
101 2005; Allen et al., 2007) and kB^{-1} (Bastiaanssen et al., 1998), or the values for the aerodynamic
102 parameters are kept constant in time and space. However, these parameters should not be
103 considered constant, nor set to zero, because this can lead to large inaccuracies in the estimates of
104 *H* (Verhoef et al., 1997a) and, consequently, of λET (Liu et al., 2007; Paul et al., 2014; Liu et al.,
105 2021). Studies have shown that kB^{-1} typically ranges from 1 to 12, depending on the dominant
106 surface coverage (Kustas et al., 1989a; Troufleau et al., 1997; Verhoef et al., 1997a; Lhomme et al.,
107 2000; Su et al., 2001). Studies confirm that if appropriate values of kB^{-1} are used, *H* can be accurately
108 estimated using LST via the bulk transfer method (Stewart et al., 1994; Su et al., 2001; Jia et al.,
109 2003; Paul et al., 2013).

110 Another problem with RS-based SEB models is that these methods are imprecise when
111 applied to non-agricultural environments, such as forests, deserts, sparse savannahs or rangelands,
112 and riparian systems, because of the heterogeneous nature of the vegetation, terrain, soils, and
113 water availability in these environments. This causes the flux estimates obtained with the SEB
114 methods, and the underlying aerodynamic parameters, to be highly variable (Allen et al., 2011;
115 Gokmen et al., 2012; Barraza et al., 2017; Chen and Liu, 2020; Costa-Filho et al., 2021). This is
116 especially true in Seasonally Dry Tropical Forests (SDTF) regions, where there is a large spatio-
117 temporal variation in vegetation density, in vegetation structural parameters such as canopy height,
118 crown shape and branching, and water availability. SDTF are an important tropical biome and one

119 of the most threatened ecoregions of the world (Moro et al., 2015; Pennington et al., 2018). SDTF
120 are broadly defined as forest formations in tropical regions characterised by marked seasonality in
121 rainfall distribution, resulting in a prolonged dry season that usually lasts five or six months
122 (Pennington et al., 2009; Paloschi et al., 2020). The most extensive contiguous areas of SDTF are
123 in the neotropics, comprising more than 60% of the remaining global stands of this vegetation (Miles
124 et al., 2006; Queiroz et al., 2017). The physiognomies exhibited by SDTF are heterogeneous, with
125 vegetation ranging from tall forests with closed canopies to scrublands rich in succulents and thorn-
126 bearing plants (Moro et al., 2015; Paloschi et al., 2020). SDTF foliage patterns are adapted to the
127 intense climate and water seasonality, which is highly dependent on interannual climate variability
128 (Alberton et al., 2017; Medeiros et al., 2022). The vegetation drops most leaves during the dry
129 season, and the first rainfall events trigger a rapid leaf growth in the wet season (Alberton et al.,
130 2017; Paloschi et al., 2020; Medeiros et al., 2022). SDTF are being rapidly degraded (12% between
131 1980 and 2000), highlighting an urgent priority for their conservation (Moro et al., 2015; Maia et al.,
132 2020). The risks faced by SDTF mainly stem from anthropogenic disturbance effects, which range
133 from local habitat loss to global climate change, leading to biodiversity loss and reductions in biomass
134 (Allen et al., 2017; Maia et al., 2020).

135 Application of SEB models to estimate evapotranspiration over SDTF has been challenging
136 due to the incompatibility between the existing assumptions of the models and the specificities of
137 these forests. Precipitation seasonality is the primary phenological regulator of SDTF (Moro et al.,
138 2016; Campos et al., 2019; Paloschi et al., 2020), and land-cover patterns show distinct intra- and
139 inter-annual spectral responses (Cunha et al., 2020; Andrade et al., 2021; Medeiros et al., 2022).
140 Therefore, biophysical remotely-sensed variables, such as Normalized Difference Vegetation Index
141 (NDVI) and surface albedo, which are usually used to select the endmembers, exhibit high spatial
142 and temporal variability in SDTF, which causes ET estimates from the SEB models to lack fidelity
143 (Silva et al., 2019). Selection of suitable roughness parameters such as z_0 , d_0 , and kB^{-1} is
144 important for the correct quantification of the energy balance in SDTF. However, these parameters
145 are more challenging to obtain in SDTF than for evergreen forests, as in addition to vegetation height,
146 other characteristics such as plant density, above-ground plant structure and the strong seasonality
147 of phenology (Alberton et al., 2017; Miranda et al., 2020; Paloschi et al., 2020) have a considerable

148 effect on the turbulent transfer in these forests. Another key issue is how to verify the results of SEB
149 methods due to the scarcity, in many regions, of terrestrial observations and the uneven
150 spatiotemporal distribution of monitoring data. SEB models may not satisfactorily represent ET in
151 regions with sparse vegetation and high climatic seasonality, such as SDTF (Senkondo et al., 2019;
152 Laipelt et al., 2021; Melo et al., 2021). The main reason is that these methods have generally been
153 evaluated and/or parameterized using sites located in other ecosystems and climates in North
154 America, Europe, Australia, East Asia, and in agricultural regions that have characteristics quite
155 distinct from SDTF (Melo et al., 2021). Therefore, a better quantification of ET, especially in regions
156 with high climatic seasonality, will help to design better water management policies that will be able
157 to deal with the effects of climate variability, land use/cover and climate changes (Lima et al., 2021).

158 We hypothesise that a SEB model that improves or considers estimates of rah via $z0m$ and
159 kB^{-1} will improve H and ET for STDF. To test this assumption, we introduce a novel calibration-free
160 SEB model based upon a one-source bulk transfer equation, herein referred to as Seasonal Tropical
161 Ecosystem Energy Partitioning (STEEP). The STEEP model aims to improve H and ET estimates
162 for STDF by incorporating the woody structure of plants through the Plant Area Index (PAI), and soil
163 moisture obtained by remote sensing to help represent the seasonality of the aerodynamic and
164 surface variables that drive the energy fluxes. To obtain the coefficients of the linear relationship
165 between dT and LST its coefficients, we computed H by the surface energy balance, and the
166 remaining λET through the principle of the Priestley-Taylor equation in the hot/dry and cold/wet
167 endmembers. STEEP is designed to take advantage of the extensive free database available on the
168 Google Earth Engine (GEE) cloud computing environment. STEEP is herein evaluated at the field
169 scale against four flux towers in the Caatinga, the largest continuous SDTF in the Americas.
170 Additionally, the model was compared with SEBAL and two consolidated global ET products: MOD16
171 (Mu et al., 2011; Running et al., 2017) and PMLv2 (Zhang et al., 2019).

172

173 **2. Methodology**

174 2.1 Study areas and respective data

175 The study concerns the Brazilian Caatinga, located between the Equator and the Tropic of
176 Capricorn (about 3 and 18° south), in the Brazilian semiarid region. It covers an area of about

177 850,000 km² (Silva et al., 2017a; Andrade et al., 2021; Brazil MMA, 2021). The climate in the
178 Caatinga is characterized by high air temperatures (around 26–30° C) and high potential
179 evapotranspiration (1,500–2,000 mm/year) coupled with low annual rainfall (300–800 mm/year,
180 normally concentrated in 3–6 months) with high intra- and inter-annual variability in space and time,
181 and a long dry season which sometimes lasts up to 11 months in some areas of Caatinga (Moro et
182 al., 2016; Miranda et al., 2018; Paloschi et al., 2020). The Caatinga vegetation has at least thirteen
183 physiognomies ranging from woods to sparse thorny shrubs, morphologically adapted to resist water
184 stress and high air temperatures (Araújo et al., 2009; Silva et al., 2017a; Marques et al., 2020;
185 Miranda et al., 2020), and it has been identified as one of the most biodiverse SDTF regions globally
186 (Pennington et al., 2006; Santos et al., 2014; Koch et al., 2017). Still, the Caatinga and other SDTF
187 are among the least studied ecoregions compared to tropical forests and savannas (Santos et al.,
188 2012; Koch et al., 2017; Tomasella et al., 2018; Borges et al., 2020). Only 1% of the Brazilian
189 Caatinga area is legally protected (Koch et al., 2017).

190 We used data from four sites located in the Caatinga (Fig. 1 and Table 1). The surrounding
191 areas of each of our study sites — which exceeds these EC towers footprints — are homogeneously
192 covered by Caatinga vegetation (Fig. S1). Located on crystalline terrain (Fig. 1a), these Caatinga
193 sites have soils with highly variable properties, ranging from fertile (those with a clayey texture) to
194 poor (those soils that are sandier). However, most soils of the SDTF are typically shallow and stony
195 (i.e. Entisols, Alfisols, and Ultisols; WRB, 2006), retaining water only for a short period between
196 rainfall events and after the rainy season (Moro et al., 2015; Queiroz et al., 2017). The wet and (dry)
197 seasons from the sites Petrolina (PTN) are concentrated in Jan–Apr (May–Dec; Souza et al., 2015);
198 Serra Negra do Norte (SNN) in Jan–May (June–Dec; Marques et al., 2020); Serra Talhada (SET) in
199 Nov–Apr (May–Oct; Silva et al., 2017b) and Campina Grande (CGR) in Mar–July (Aug–Feb; Oliveira
200 et al., 2021). The climate of the four observation sites is semi-arid, type BSh (Fig. 1b) according to
201 the Köppen climate classification (Alvares et al., 2013).

202 Eddy covariance data, covering several periods from 2011 to 2020 (Fig. 1c), were used to
203 evaluate the modelled ET and *H*. The four sites were instrumented with five flux towers equipped
204 with three-dimensional ultrasonic anemometers (CSAT3, Campbell Scientific Inc., Logan, UT, USA
205 in all the sites except CGR 2020) and open-path infrared gas analysers (LI-7500, LI-COR Inc.,

206 Lincoln, NE, USA, in the PTN site, or EC150, Campbell Scientific Inc., Logan, UT, USA, in the SET,
207 SNN, and CGR 2014 sites). In the more recent experiment (CGR 2020), the flux tower was equipped
208 with an IRGASON (Campbell Scientific Inc., Logan, UT, USA) that integrates the two sensors in just
209 one instrument. ET data for the PTN, SNN, and SET sites have been previously described; they
210 underwent standard procedures to ensure their quality and were published by Melo et al. (2021).
211 Observations at the CGR site were collected through two micrometeorological towers, located in a
212 dense Caatinga area within the Brazilian National Institute of Semiarid (INSA) experimental area, a
213 300 ha forest reserve with different stages of regeneration. The first tower (height of 7 m) was active
214 between the years of 2014 and 2017, as described in Oliveira et al. (2021). The second tower (height
215 of 15 m) is part of the Caatinga Observatory (OCA) and includes an EC system that has been
216 collecting data since 2020. The OCA is a laboratory maintained by the Federal University of Campina
217 Grande and INSA. H data for the PTN, SNN and CGR sites have been obtained from the respective
218 principal investigators, while data for the SET site have been obtained from the AmeriFlux network
219 (Antonino, 2019). For the retrieval of λET and H , LoggerNet software (Campbell Scientific, Inc.,
220 Logan, UT, USA) was used in order to transform 10 Hz raw data into 30 min binaries. Afterwards,
221 EdiRe software (Campbell Scientific Inc., Logan, UT, USA) was used to process the high-frequency
222 data, averaging every 30 min. The data from the EC flow towers in CGR have previously gone
223 through standard procedures to ensure their quality. Detailed information on data processing, quality
224 control, and post-processing can be found in Campos et al. (2019) and Cabral et al. (2020). The raw
225 data from the CGR flux tower were processed by Easy-flux data processing software (Campbell
226 Scientific Inc., Logan, UT, USA). In addition, data for any day with rainfall greater than 0.5 mm were
227 removed. The daily ET was calculated using the daily average λET .

228

229

230

231

232

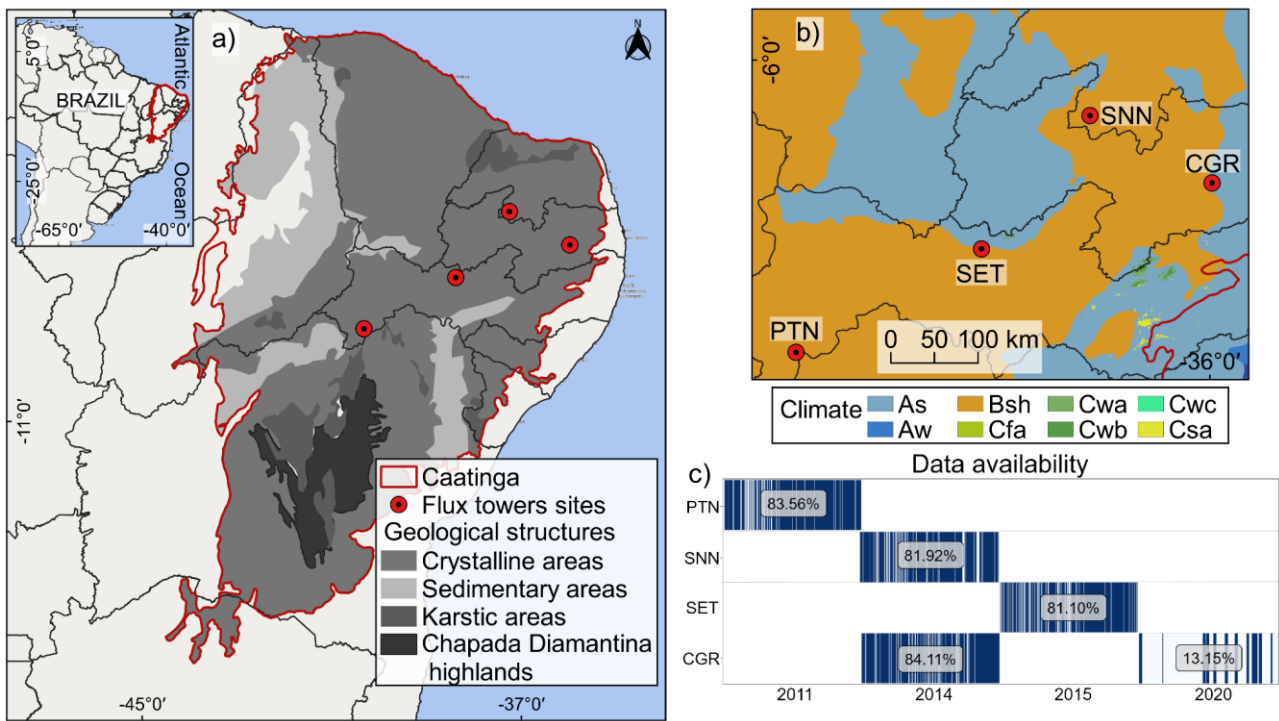
233

234 Table 1. List of EC-equipped flux tower observation sites in the study area.

Sites	State of Brazil	Mean annual of rainfall (mm) ¹	Site average elevation (m)	Main tree species	Location (Lon;Lat)	Data availability	Wet / Dry Seasons	Main reference
Petrolina (PTN)	Pernambuco	428.6	395	<i>Commiphora leptophloeos</i> , <i>Schinopsis brasiliensis</i> , <i>Mimosa tenuiflora</i> , <i>Cenostigma microphyllum</i> , <i>Sapium glandulosum</i>	-40.3212; -9.0465	Jan–Dec 2011	Jan-Apr / May-Dec	Souza et al. (2015)
Serra Negra do Norte (SNN)	Rio Grande do Norte	629.5	205	<i>Caesalpinia pyramidalis</i> , <i>Aspidosperma pyriformis</i> , <i>Anadenanthera colubrina</i> , <i>Croton blanchetianus</i>	-37.2514; -6.5783	Jan–Dec 2014	Jan-May / June-Dec	Marques et al. (2020)
Serra Talhada (SET)	Pernambuco	648	465	<i>Mimosa hostilis</i> , <i>Mimosa verrucosa</i> , <i>Croton sonderianus</i> , <i>Anadenanthera macrocarpa</i> , <i>Spondias tuberosa</i>	-38.3842; -7.9682	Jan–Dec 2015	Nov-Apr / May-Oct	Silva et al. (2017b)
Campina Grande (CGR)	Paraíba	777	490	<i>Croton blanchetianus</i> , <i>Mimosa ophthalmocentra</i> , <i>Poincianella pyramidalis</i> , <i>Allophylus quercifolius</i> , <i>Mimosa sp.</i> ²	-35.9750; -7.2798	Jan–Dec 2014	Mar-July / Aug-Feb	Oliveira et al. (2021)
Campina Grande (CGR)	Paraíba	777	490	<i>Croton blanchetianus</i> , <i>Mimosa ophthalmocentra</i> , <i>Poincianella pyramidalis</i> , <i>Allophylus quercifolius</i> , <i>Mimosa sp.</i> ²	-35.9763; -7.2805	Jan–Dec 2020	Mar-July / Aug-Feb	This study

235 ¹ Rainfall Data Sources: Brazilian National Institute of Meteorology (INMET) and Pernambuco State Agency for Water and Climate (APAC).

236 ² Barbosa et al. (2020).



237

238

239

240

241

242

243

244

245

246

247

248

249

250

251

252

253

254

Fig. 1. Location of flux tower observation sites in Caatinga. a) Geographical overview of the

Caatinga (Moro et al., 2015), b) Köppen's climate classification map: Tropical zone with dry summer

(As), Tropical zone with dry winter (Aw), Dry zone semi-arid low latitude and altitude (Bsh), Humid

subtropical zone without dry season and with hot summer (Cfa), Humid subtropical zone with dry

winter and hot summer (Cwa), Humid subtropical zone with dry winter and temperate summer

(Cwb), Humid subtropical zone with dry winter and short and cool summer (Cwc), Humid

subtropical zone with dry summer and hot (Csa), according to Alvares et al. (2013) and c) Data

availability on the observation sites after procedures to ensure their quality.

2.2 The Seasonal Tropical Ecosystem Energy Partitioning (STEEP) model

SEB models have been applied in many parts of the world (Mohan et al., 2020a). The one-

source SEB models that are most commonly found in the literature are SEBAL (Bastiaanssen et al.,

1998), Surface Energy Balance System (SEBS; Su, 2002), Mapping EvapoTranspiration at high

Resolution with Internal Calibration (METRIC; Allen et al., 2007), and Operational Simplified Surface

Energy Balance (SSEBop; Senay et al., 2013). As in other SEB models, STEEP performs the energy

balance at the time of satellite overpass (instantaneous) to obtain λET as the surface energy balance

residual. The computation of R_n and G , necessary to get λET , followed the procedures described in

Ferreira et al. (2020) and Bastiaanssen et al. (2002), respectively, but with input data from the

255 Moderate-Resolution Imaging Spectroradiometer (MODIS) sensor. H was calculated following the
256 methods described in Table 2: using rah and dT , both traditionally applied in SEB models, but also
257 focusing on peculiarities of SDTF that have never been considered in other SEB models. In this
258 proposed version, rah was described according to Verhoef et al. (1997a) and Paul et al. (2013),
259 which requires, among other parameters/variables, the momentum roughness length ($z0m$), the zero
260 plane displacement height ($d0$), the dimensionless parameter kB^{-1} , and the atmospheric stability
261 corrections (Paulson, 1970). $z0m$ is influenced by a range of plant structural properties, e.g.
262 vegetation height, breadth and vegetation drag coefficients, and spacing (or density). $z0m$ is
263 commonly computed as a function of Leaf Area Index (LAI; Verhoef et al., 1997b; Liu et al., 2021).
264 However, most SDTF plants spend a substantial part of the year without leaves; under these
265 conditions, $z0m$ should be derived from information on dimensions of trunks, stems, and branches.
266 Since LAI is only related to leaf cover quantity and variability, it cannot represent the woody plant
267 structure without leaves (Miranda et al., 2020). Therefore, the Plant Area Index (PAI), which is the
268 total above-ground plant area, i.e. leaves and woody structures, was used to represent plant
269 structures in the computation of $z0m$ and $d0$.

270 To incorporate the conditions of water variability in the forest system in the calculation of
271 sensible heat we applied the procedure described in Gokmen et al. (2012) that corrects the kB^{-1}
272 equation presented in Su et al. (2001), incorporating soil moisture obtained by remote sensing. The
273 canopy conductance profiles are the link between soil moisture and sensible/latent heat flux. The
274 source of sensible/latent heat moves vertically throughout the canopy as a function of plant water
275 stress (Gokmen et al., 2012; Bonan et al., 2021), which affects heat roughness length, and, therefore,
276 kB^{-1} and rah . Thus, when there is a reduction in soil moisture, there is also a reduction in the value
277 of rah and, consequently, an increase of H and a decrease in λET . Furthermore, to calculate dT , we
278 used the linear relationship on LST, using the assumption of extreme contrast in terms of cover and
279 soil wetness (hot/dry and cold/wet endmembers) to determine the linear relationship coefficients.
280 However, in the hot/dry and cold/wet endmembers pixels, H was computed by the surface energy
281 balance (Allen et al., 2007), and the remaining λET was incorporated through the Priestley-Taylor
282 (1972) equation and plant physiological constraints following the approach in Singh and Irmak (2011)
283 and French et al. (2015). PAI and soil moisture time series used in our study can be seen in Fig. S2.

284 The references for the methods and equations adopted to formulate the STEEP model can be found
 285 in Table 2 and Appendix A, respectively. For illustration purposes, Table 2 also shows the references
 286 for the methods for one of the most widely used RS SEB models, the SEBAL model.

287 Table 2. References for the methods used in the STEEP and SEBAL models to obtain the sensible
 288 heat flux.

Variable/Parameter	STEPP	SEBAL
Aerodynamic resistance for heat transfer (rah)	Verhoef et al., 1997a; Paul et al., 2013	Bastiaanssen et al., 2002; Laipelt et al., 2021
Roughness length for momentum transfer ($z0m$)	Verhoef et al., 1997b; Paul et al., 2013, replacing LAI with PAI	Bastiaanssen et al., 2002; Laipelt et al., 2021
Zero plane displacement height ($d0$)	Verhoef et al., 1997b; Paul et al., 2013	-
Plant Area Index (PAI)	Miranda et al., 2020	-
Parameter kB^{-1}	Su et al., 2001	uses $z0h$ with constant value (0.1); Bastiaanssen et al., 2002
Correction of soil moisture by remote sensing in kB^{-1}	Gokmen et al., 2012	-
Calculation of the H and the remaining λET in endmembers pixels	Allen et al., 2007; Singh and Irmak, 2011; French et al., 2015	Calculation of the H in the hot/dry endmember only; Bastiaanssen et al., 2002

289

290 2.3 Algorithm implementation and processing

291 We implemented STEEP on the Google Earth Engine (GEE) cloud computing environment
 292 (Gorelick et al., 2017) using the Python API (version 3.6). Statistical analyses to evaluate the
 293 performance of the models were also conducted in Python and implemented in the Jupyter
 294 programming environment. The Python package geemap (Wu, 2020) enabled the integration of
 295 Python with the GEE environment, and the hydrostats package (Roberts et al., 2018) was used for
 296 the statistical evaluation of the performance of the models.

297 We designed the application of the model to take advantage of the data available on GEE
 298 (Table 3). The remote sensing datasets were derived from MODIS sensor products, the Shuttle
 299 Radar Topography Mission (SRTM; Farr et al., 2007), and the Global Forest Canopy Height product
 300 provided vegetation height (Potapov et al., 2021). The climate data necessary to run the model, i.e.
 301 wind speed, air temperature, relative humidity, shortwave radiation, and net thermal radiation at the
 302 surface, were sourced from the ERA5-Land reanalysis product (Muñoz Sabater, 2019). For data

303 regarding soil moisture, we used the Global Land Data Assimilation System (GLDAS) product
 304 (Rodell et al., 2004). CHIRPS precipitation product (Funk et al., 2015) was used to estimate the daily
 305 rainfall amount at the sites evaluated.

306 Table 3. Description of the datasets available on the GEE platform used in the research.

Product	GEE ID	Bands/variables	Time coverage	Spatial resolution	Temporal resolution
MCD43A4.006	MODIS/006/ MCD43A4	B1–B7	Feb 2000– present	0.5 km	1 day
MOD09GA.006	MODIS/006/ MOD09GA	SolarZenith	Feb 2000– present	1 km	1 day
MOD11A1.006	MODIS/006/ MOD11A1	LST_Day_1km; Emis_31, Emis_32	Mar 2000– present	1 km	1 day
SRTM	USGS/SRT MGL1_003	Elevation	Feb 2000	0.03 km	-
ERA5-Land	ECMWF/ER A5_LAND/H OURLY	dewpoint_temperature_2m, temperature_2m, u_component_of_wind_10, v_component_of_wind_10m, surface_net_solar_radiation _hourly, surface_net_thermal_radiati on_hourly	Jan 1981– present	0.1°	1 h
GLDAS	NASA/GLDA S/V021/NOA H/G025/T3H	SoilMoi0_10cm_inst	Jan 2000– present	0.25°	3 h
Global Forest Canopy Height, 2019	users/potapo vpeter/GEDI _V27	-	Apr 2019	0.03 km	-
CHIRPS	UCSB- CHG/CHIRP S/DAILY	Precipitation	Jan 1981– present	0.05°	1 day
MOD16A2.006	MODIS/006/ MOD16A2	ET	Jan 2001– present	0.5 km	8 days
PML_V2	projects/pml _evapotrans piration/PML /OUTPUT/P ML_V2_8da y_v016	Es, Ec, Ei	Feb 2000– present	0.5 km	8 days

307
 308 The presence of clouds or instrumental malfunctioning of orbital sensors can cause gaps in
 309 data. To reduce the loss of information due to missing data, we chose to use the MODIS MCD43A4

310 reflectance product. By combining reflectance data from MODIS sensors aboard the AQUA and
311 TERRA satellites and modelling the anisotropic scattering characteristics using sixteen-day quality
312 observations, the MCD43A4 product represents the daily dynamics of the Earth's surface without
313 missing data (Schaaf and Wang, 2015). Daily surface reflectance data from the MCD43A4 product
314 were used to obtain the surface albedo and vegetation indices (NDVI and PAI) needed to run STEEP.
315 Thus, the surface albedo data and the vegetation indices show a low percentage of missing data.
316 To compose the LST time series, we used data from MOD11A1, and to fill its missing data, a filter
317 with the average value for a monthly window was applied. This procedure is similar to the method
318 proposed by Zhao et al. (2005) and it is also used by the MOD16 algorithm to generate the
319 continuous global ET (Mu et al., 2011).

320 Following the approach in comparable studies, STEEP algorithm processing was conducted
321 with automatic selection of endmembers pixels (Bhattarai et al., 2017; Silva et al., 2019; Laipelt et
322 al., 2021). Like Silva et al. (2019), we used the biophysical variables NDVI, surface albedo and LST
323 to automate selection of the endmembers, but we applied different criteria. For the hot/dry
324 endmember selection, the first step consisted of selecting those pixels whose surface albedo values
325 are between the 50 and 75% quantiles, and with NDVI values greater than 0.1 and less than the
326 15% quantile. After this first selection, a refinement is applied by selecting only those pixels from this
327 first set that have LST values between the 85 and 97% quantiles. Using the set of pixels that met
328 these criteria, the median values of R_n , G , LST and rah were calculated to establish a single value
329 for each variable and describe the characteristics of the hot pixel. We applied a similar procedure to
330 select the cold/wet endmember but with different limits (Table 4). The procedure for finding
331 endmembers was conducted daily. To execute the model and conduct the selection of endmembers,
332 we used an area of interest (AOI), also known as domain size. AOI was defined as a square area
333 with 1000-km sides within the Caatinga domain and centred on the tower coordinates of each site.
334 Cheng et al. (2021), for example, applied the SEBAL using MODIS data in China and used an AOI
335 of 1200-km x 1200-km.

336 Table 4. Methodology used for the selection of endmembers pixels.

Endmembers

	Hot/dry pixel	Cold/wet pixel
Step 1	Q50% < surface albedo < Q75% and 0.10 < NDVI < Q15%	Q25% < surface albedo < Q50% and NDVI > Q97%
Step 2	of the pixels of the 1st Step, select pixels with Q85% < LST < Q97%	of the pixels of the 1st Step, select pixels with LST < Q20%
Step 3	Of the set of pixels that met the previous steps, the median values of R_n , G , LST and rah were calculated to establish a single value for each variable and describe the characteristics of endmembers	

337 Q = quantile.

338 2.4 Analysis of the algorithms' performance

339 We used SEBAL as a reference RS SEB model for comparison with STEEP. SEBAL is one
340 of the most applied SEB models since the algorithm uses a minimal number of in situ measurements
341 compared to similar models, e.g. METRIC and SSEBop, and is considered a suitable choice for
342 evapotranspiration estimates over cropped areas and in the context of water resource management
343 (Kayser et al., 2022). Applications with SEBAL have been conducted in the Caatinga as in the studies
344 of Teixeira et al. (2009), Santos et al. (2020), Costa et al. (2021), and Lima et al. (2021).
345 Implementations of the SEBAL algorithm are popular on several computing platforms, e.g. GRASS-
346 Python (Lima et al., 2021); Google Earth Engine (Laipelt et al., 2021); Python (Mhawej et al., 2020),
347 following the formulations described in Bastiaanssen et al. (1998) and Bastiaanssen et al. (2002).
348 The SEBAL version implemented in this work followed those presented by Bastiaanssen et al.
349 (2002), Costa et al. (2021) and Laipelt et al. (2021). The remote sensing datasets and endmembers
350 pixels selection for SEBAL were the same as described in STEEP.

351 ET and H estimates from STEEP and SEBAL were evaluated against the eddy covariance
352 measurements of the corresponding tower. Here, the modelled values were extracted for the pixel
353 representing the EC tower for each observation site. The footprint fetches for PTN, SET, SNN is less
354 than 500 m (Silva et al., 2017b; Campos et al., 2019; Santos, et al., 2020). We assume a similar
355 footprint for CGR due to its similarity in terms of wind characteristics and terrain slope compared to
356 the other sites. Moreover, the surrounding areas of each of our study sites (Fig. S1) — which exceeds
357 these EC towers footprints — are homogeneously covered by Caatinga vegetation. We evaluated
358 daily ET values, and instantaneous hourly H values more specifically with the modelled/measured H

359 value at 11:00 am local time (GMT-3), considering this is the closest time to the satellite's overpass.
360 Additionally, the STEEP model was compared with two consolidated global ET products available
361 on GEE: MODIS Global Terrestrial Evapotranspiration A2 version 6 (MOD16; Mu et al., 2011;
362 Running et al., 2017) and Penman-Monteith-Leuning model version 2 global evaporation (PMLv2;
363 Zhang et al., 2019); both products have a pixel resolution of 500 m (Table 3). The algorithm used in
364 MOD16 is based on the Penman-Monteith equation and driven by MODIS remote sensing data with
365 Modern-Era Retrospective analysis for Research and Applications (MERRA; Mu et al., 2011). In
366 MOD16 ET is the sum of soil evaporation (E_s), canopy transpiration (T_c) and wet-canopy evaporation
367 (E_c) and is provided as eight-day *cumulative* values. More details about MOD16 can be found in Mu
368 et al. (2011) and Running et al. (2017). The global PMLv2 product involves a biophysical model
369 based on the Penman-Monteith-Leuning equation which also uses MODIS remote sensing data, but
370 with meteorological reanalysis data from GLDAS as model inputs. As in MOD16, ET in PMLv2 is
371 also the sum of E_s , T_c and E_c but is provided as eight-day *average* values. To make MOD16 and
372 PMLv2 values compatible, ET of PMLv2 was multiplied by eight. Details about PMLv2 can be found
373 in Gan et al. (2018) and Zhang et al. (2019). We accumulated the daily ET measured at the
374 observation sites, i.e. derived from EC data, and ET modelled with STEEP for the same eight-day
375 time periods to make them compatible with the temporal resolution of the MOD16 and PMLv2
376 datasets. The average of the measured daily values over each eight-day time period (even if there
377 were missing values within this period) was multiplied by eight to calculate the observed 8-day ET.
378 To match the time steps of STEEP and MOD16/PMLv2 ET values, the 8-day average of the
379 evaporative fraction (EF) was multiplied by the daily net radiation over those 8 days, assuming that
380 EF can be considered constant in each of these periods. Then the ET was summed over the 8-day
381 interval. Finally, we also compared the modelled ET (by STEEP and the two global products) with
382 the observed ET, only in the 8-day periods when no field-observed data was missing. However, with
383 this criterion the number of observations dropped dramatically.

384 The STEEP and SEBAL models and global ET products were evaluated with five performance
385 metrics (Table 5). A combination of performance metrics is often used to assess the overall
386 performance of models because a single metric provides only a projection of a certain aspect of the
387 error characteristics (Chai and Draxler, 2014). Root mean square error (*RMSE*) is commonly used

388 to express the accuracy of the results with the advantage that it presents error values in the same
389 units of the variable analysed; optimal values are close to zero (Hallak and Pereira Filho, 2011).
390 Coefficient of determination (R^2) represents the quality of the linear trend between observed and
391 simulated data and ranges from 0 to 1; high values indicate better model performance. Nash–
392 Sutcliffe efficiency (NSE) indicates the accuracy of the model output compared to the average of the
393 referred data ($NSE = 1$ is the optimal value; Nash and Sutcliffe, 1970). Concordance correlation
394 coefficient (ρc) is a measure that evaluates how well bivariate data falls on the 1:1 line. ρc measures
395 both precision and accuracy. It ranges from -1 to +1 similar to Pearson's correlation coefficient, with
396 perfect agreement at +1 (Lin, 1989; Liao and Lewis, 2000; Akoglu, 2018). Percentage bias ($PBIAS$)
397 measures the average relative difference between observed and estimated values, with an optimal
398 value of 0 (Gupta et al., 1999). Additionally, we evaluate STEEP's model structure by extracting
399 model's performance metrics after excluding it from its main implementations individually (Table 2)
400 and by two-by-two combinations of zOm , rah and $r\lambda ET$. We run the control version of the SEB model,
401 i.e. SEBAL in our case, while incorporating one or two improvements in the model and keeping the
402 remaining parts of the algorithm the same as the reference SEB model.

403 Table 5. Performance metrics used to evaluate ET and H in this study.

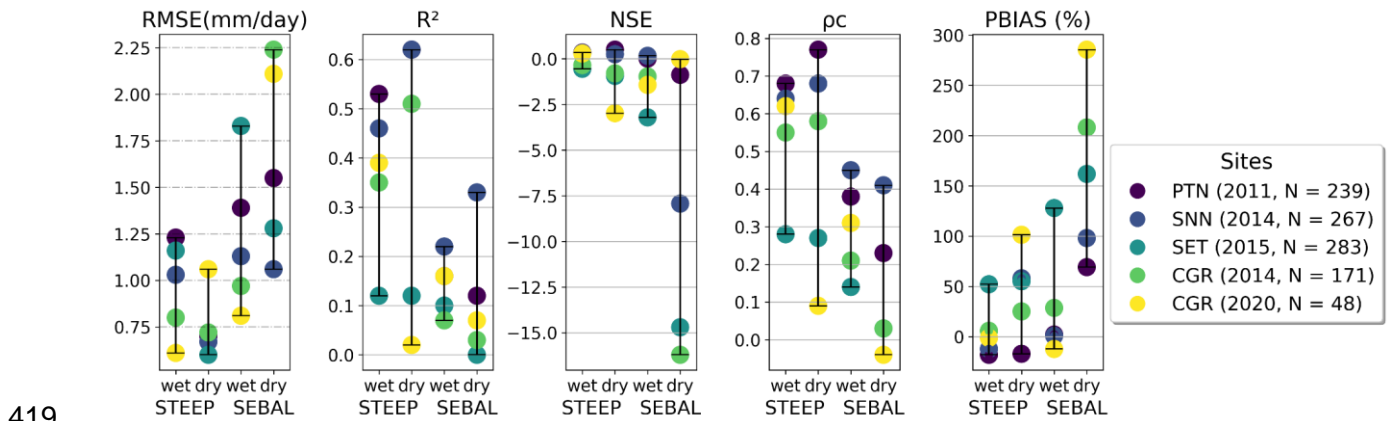
Performance metric	Equation	Range (Perfect value)
Root mean square error ($RMSE$)	$RMSE = \sqrt{\frac{\sum_{i=1}^N (M_i - O_i)^2}{N}}$	$[0, +\infty [(0)$
Coefficient of determination (R^2)	$R^2 = \frac{[\sum_{i=1}^N (O_i - \bar{O})(M_i - \bar{M})]^2}{\sum_{i=1}^N (O_i - \bar{O})^2 \cdot \sum_{i=1}^N (M_i - \bar{M})^2}$	$[0, 1] (1)$
Nash–Sutcliffe efficiency (NSE)	$NSE = 1 - \frac{\sum_{i=1}^N (M_i - O_i)^2}{\sum_{i=1}^N (O_i - \bar{O})^2}$	$]-\infty, 1] (1)$
Concordance correlation coefficient (ρc)	$\rho c = \frac{2 \sum_{i=1}^N (O_i - \bar{O})(M_i - \bar{M})}{\sum_{i=1}^N (O_i - \bar{O})^2 + \sum_{i=1}^N (M_i - \bar{M})^2 + (N - 1)(\bar{O} - \bar{M})^2}$	$[-1, 1] (1)$
Percentage bias ($PBIAS$)	$PBIAS = \frac{\sum_{i=1}^N (M_i - O_i) \cdot 100}{\sum_{i=1}^N O_i}$	$]-\infty, +\infty [(0)$

404 where: N sample size; O observed value; M modelled value; \bar{O} observed mean; \bar{M} modelled mean.

405 3. Results and discussion

406 3.1 Comparison of STEEP and SEBAL models results with observed (EC) values

407 The performance statistics of daily ET by STEEP and SEBAL in wet and dry seasons for the
 408 evaluated sites are shown in Fig. 2. In general, STEEP exhibited a better performance than SEBAL.
 409 Although the better statistical metrics of STEEP were in the dry season, in the wet season, they were
 410 also superior compared to SEBAL. Specifically, in the dry season, STEEP exhibited a *RMSE*
 411 between 0.6 and 1.06 mm/day, while SEBAL this was between 1.06 and 2.24 mm/day. The maximum
 412 value of R^2 in STEEP was 0.62 (sites PTN and SNN), whereas SEBAL achieved only 0.33. The *NSE*
 413 metric was the worst among the five analysed in SEBAL: values lower than -7.5 occurred in three of
 414 the five sites. Although in STEEP, PTN and SNN sites *NSE* had values higher than 0 (0.55 and 0.25,
 415 respectively) the other sites also had negative values, reaching up to -2.5. In terms of ρ_c , values
 416 ranged from 0.09 to 0.77 in STEEP and from -0.04 to 0.41 in SEBAL. It is also possible to see the
 417 reduction that STEEP has brought to ET modelling in terms of *PBIAS* when compared to SEBAL.
 418



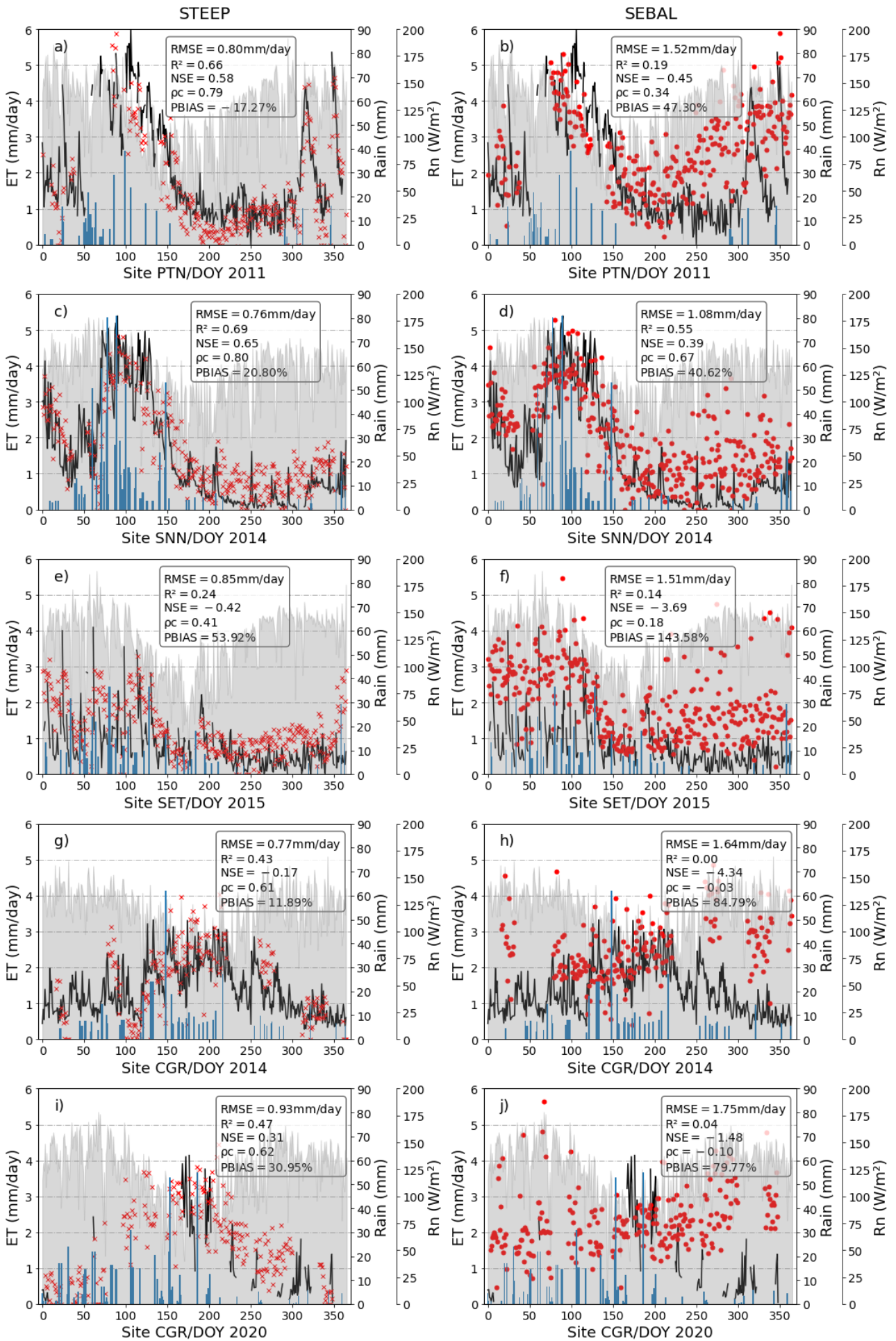
420 Fig. 2. Results of the performance statistics of daily ET in wet and dry seasons for evaluated sites.

421 Globally, without discriminating between wet and dry seasons, STEEP exhibited better
 422 statistical performance than SEBAL at all the evaluated sites (Fig. 3). While STEEP exhibited a
 423 *RMSE* between 0.75 and 0.94 mm/day, the *RMSE* for SEBAL was between 1.08 and 1.75 mm/day.
 424 In terms of R^2 , the values were between 0.24 to 0.69 for STEEP, and were below 0.2 for SEBAL for
 425 all sites except in SNN (0.55). Similarly, *NSE* and ρ_c values were higher for STEEP compared to
 426 SEBAL. For STEEP, all sites had *NSE* and ρ_c values above -0.42 and 0.41, respectively, whereas
 427 all sites except SNN had values below these limits for SEBAL. Both models overestimated ET
 428 ($PBIAS > 0$), with the exception of the STEEP estimates for the PTN site. The highest overestimation
 429 by the STEEP model was less than 60%, whereas in SEBAL it was greater than 140%.

430 SEBAL metrics concerning the modelled ET were similar to those found in other studies.
431 Laipelt et al. (2021) found R^2 ranging from 0.18 to 0.87 when applying SEBAL and comparing it with
432 data from ten EC towers located in different Brazilian biomes (Amazon, Cerrado, Pantanal, and
433 Pampa). Cheng et al. (2021) obtained R^2 of 0.53–0.77 and $RMSE$ of 0.89–1.02 mm/day when
434 comparing estimates from SEBAL and EC towers on different land covers in China. Costa et al.
435 (2021), when applying SEBAL in the Caatinga, found R^2 and NSE values of 0.57 and 0.36,
436 respectively. Santos et al. (2020) modelled ET with SEBAL at the SNN site for the 2014–2016 period
437 and obtained R^2 and $RMSE$ values of 0.28 and 1.43 mm/day, respectively. For this site, we obtained
438 R^2 and $RMSE$ of 0.55 and 1.08 mm/day, respectively, for the year 2014 using SEBAL.

439 STEEP exhibited a greater seasonal accuracy compared to SEBAL (Fig. 3), as evidenced by
440 the goodness-of-fit between simulated and observed values expressed by the NSE indicator. STEEP
441 estimates followed the same temporal evolution as the observed values. STEEP satisfactorily
442 captured both minimum and maximum ET values, including after rainfall events, this is particularly
443 evident in Fig. 3a, where the two observed ET peaks in late 2011 — between DOY 300 and 360 —
444 in the PTN site were captured nicely by STEEP. This improved performance can be explained
445 because soil moisture is incorporated in the STEEP algorithm. In semi-arid regions and particularly
446 in the SDTF, besides the availability of energy, evapotranspiration is highly dependent on the soil–
447 water availability (Lima et al., 2012; Carvalho et al., 2018; Mutti et al., 2019; Paloschi et al., 2020).
448 In rainy months, low daily ET rates are often observed due to the reduced levels of incoming radiation
449 caused by high cloud cover (Mutti et al., 2019; Paloschi et al., 2020). Towards the end of the wet
450 period, when the available energy increases, the daily ET values also increase as a result of the high
451 soil water availability from previous precipitation events (Allen et al., 2011; Marques et al., 2020). In
452 the transition period from the rainy to the dry season, the leaves do not fall immediately (see Table
453 1, main tree species). Instead, leaf-shedding depends on the environmental conditions in each
454 location, including the rainy season duration, and species composition (Lima and Rodal, 2010; Lima
455 et al., 2012; Miranda et al., 2020; Paloschi et al., 2020; Queiroz et al., 2020; Medeiros et al., 2022).
456 The remaining water available in the soil or previously accumulated in plant tissues is sufficient for
457 the Caatinga vegetation to maintain its leaves, for short periods, at levels similar to the rainy season
458 (Barbosa et al., 2006; Mutti et al., 2019). However, in the dry season, when soil moisture reaches its

459 lowest levels, the Caatinga vegetation enters a state of dormancy that is accompanied by leaf drop
460 and a drastic reduction of photosynthetic activity (and hence of transpiration) as a strategy to cope
461 with the lack of available soil moisture (Dombroski et al., 2011; Paloschi et al., 2020). This resilience
462 mechanism is typical of xerophytic and/or deciduous species such as those found in the Caatinga
463 (Lima et al., 2012; Mutti et al., 2019; Paloschi et al., 2020), and explains the low rates of ET in the
464 dry season. In contrast, in SEBAL, which does not consider water availability, it was observed that
465 the daily ET followed the course of the daily net radiation throughout the year, especially in the dry
466 period of each of the experimental sites. This is in agreement with the results of Kayser et al. (2022),
467 who pointed out that estimates with SEBAL can be seasonally accurate in locations where the main
468 driver of ET is the available energy. Our results highlight that SEB models such as SEBAL, which
469 are formulated to be mainly dependent on energy availability and do not consider soil and plant water
470 availability, may not satisfactorily represent ET in semi-arid vegetation such as that found in the
471 SDTF (Gokmen et al., 2012; Paul et al., 2014; Melo et al., 2021).

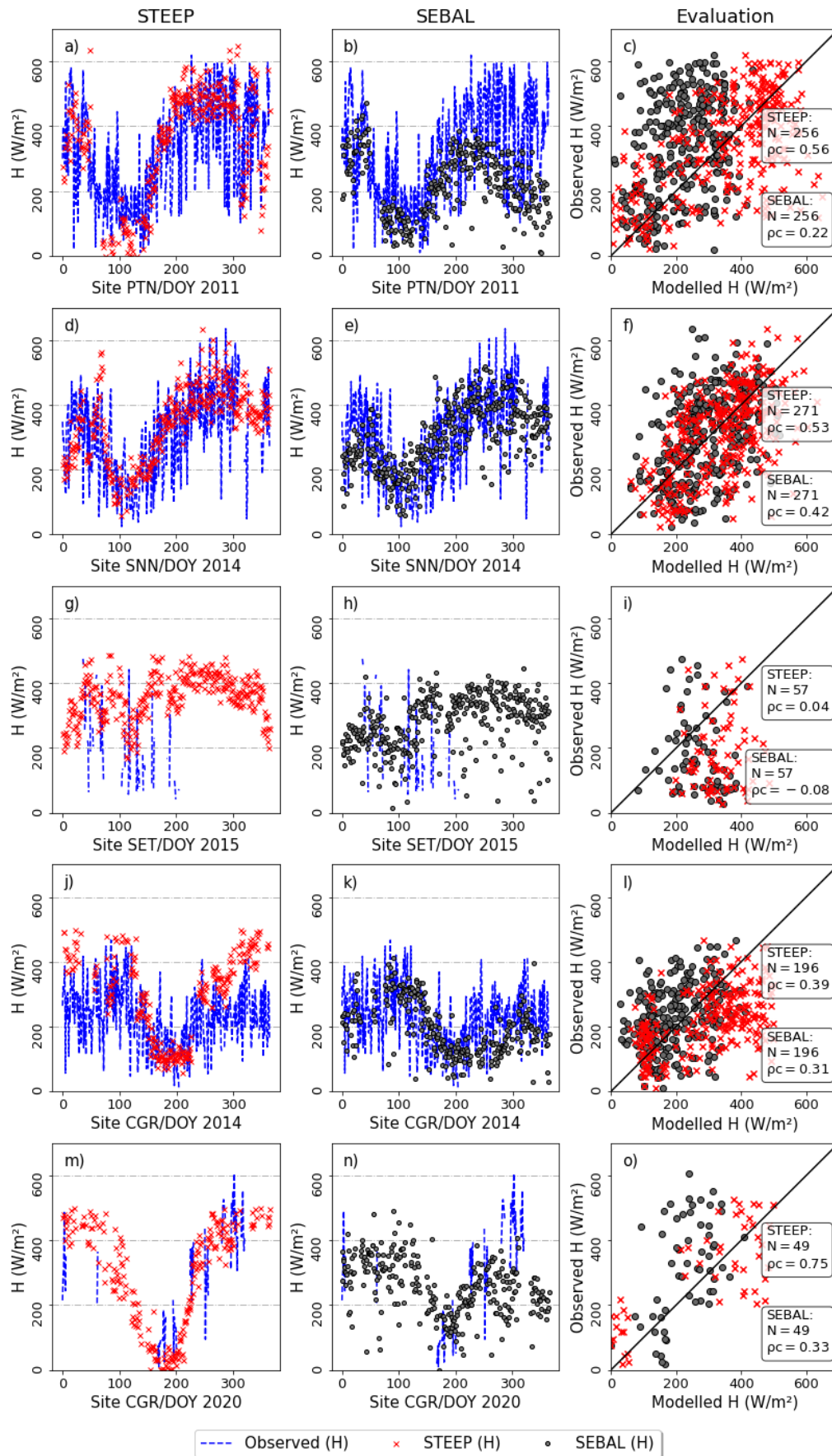


— Observed ET × STEEP • SEBAL ■ RAIN - CHIRPS ■ Daily net radiation

473 Fig. 3. Observed and modelled daily evapotranspiration (ET, mm/day) for the different
474 experimental sites: a) and b) PTN 2011, c) and d) SNN 2014, e) and f) SET 2015, g) and h) CGR
475 2014, i) and j) CGR 2020. The black lines represent observed ET; the red crosses and points are
476 STEEP and SEBAL estimates, respectively; the blue bars represent CHIRPS daily rainfall; the gray
477 region represents daily net radiation from ERA5-land.

478 The core of the STEEP and SEBAL algorithms is based on finding λET as the residual of the
479 energy balance; however, they differ with regards to the approach used to calculate H . In the STEEP
480 model, the seasonal variation of H fitted the observed values of the instantaneous measurements at
481 11:00 am (local time) better than SEBAL, for all the sites (Fig. 4). Our results show that an
482 improvement in H leads to a correspondent in ET estimates. This is contrary to the findings of Faivre
483 et al. (2017), who used the same formulation for kB^{-1} applied in our study, but included four different
484 methods to compute $z0m$. While STEEP estimates of H exhibited ρc values over 0.5 for three of the
485 five sites, SEBAL H estimates exhibited ρc values below 0.5 for all sites. When wet and dry seasons
486 data are analysed separately (Fig. 5), the same trend is observed in the results: in general, the
487 STEEP model presents better statistical metrics than SEBAL.

488



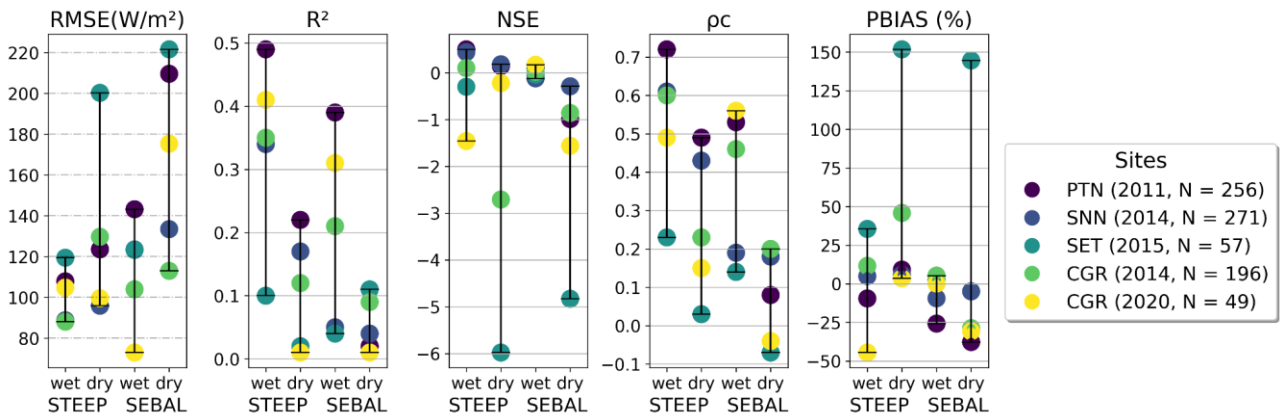
489

490

491

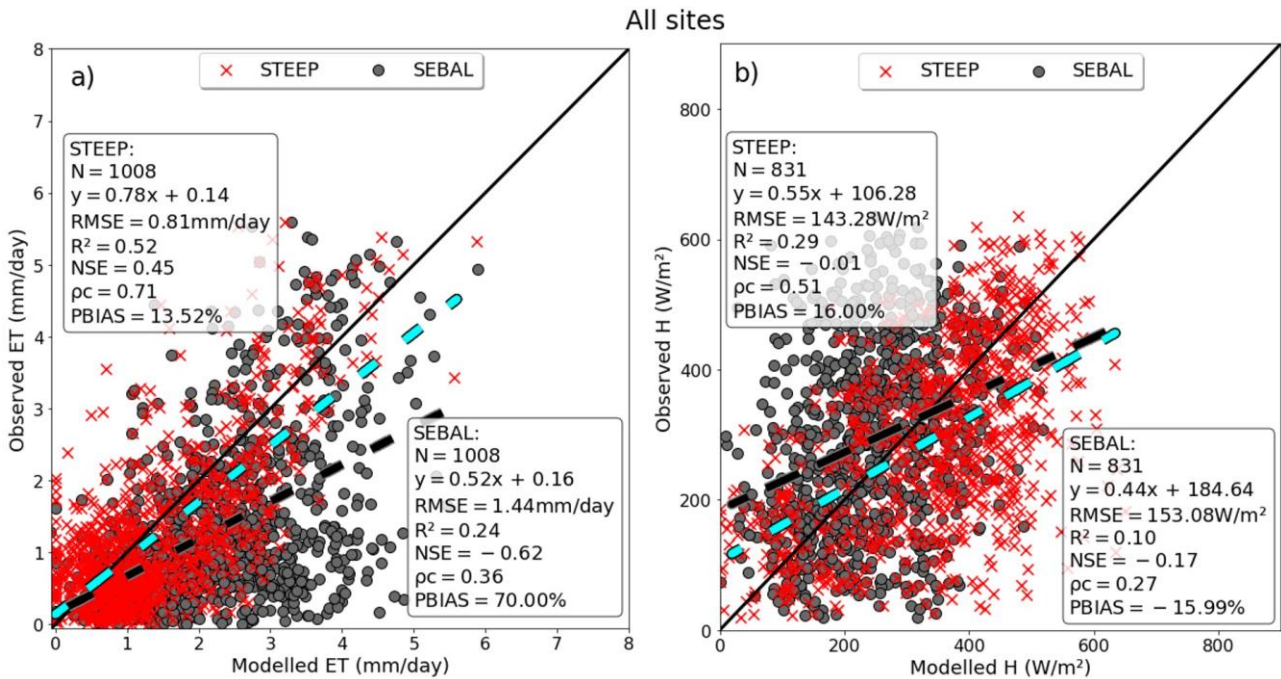
Fig. 4. Observed and modelled instantaneous sensible heat flux (H , at 11:00 am, W/m^2) for the different experimental sites: a), b) and c) PTN 2011, d), e) and f) SNN 2014, g), h) and i) SET

492 2015, j), k) and l) CGR 2014, m), n) and o) CGR 2020. The blue line represents the observed
 493 values; the red crosses and grey points correspond to the STEEP and SEBAL estimates,
 494 respectively. The black line is the 1:1 line.



495
 496 Fig. 5. Results of the performance statistics of instantaneous sensible heat flux (H , at 11:00 am,
 497 W/m^2) in wet and dry seasons, for the evaluated sites.

498 Evaluation of the STEEP and SEBAL daily ET and instantaneous H for all experimental sites
 499 (Fig. 6) indicates that both models lack a high performance for H estimates, although the use of
 500 STEEP resulted in better statistical measures than when SEBAL was employed (Fig. 6b). This
 501 substantiates previous findings (Gokmen et al., 2012; Paul et al., 2014; Trebs et al., 2021), that have
 502 shown the tendency of underestimation (overestimation) of H (ET) at water-limited sites. It can be
 503 seen that the overestimation of H by the STEEP model, compared to SEBAL, produced modelled
 504 ET values that were closer to the EC measurements (see Fig. 3 and 4). We ascribe the poor
 505 performance of H in the models relative to observed data to the continuous H oscillations throughout
 506 the day (Campos et al., 2019; Lima et al., 2021). As we compare an instantaneous H estimate
 507 (STEAP or SEBAL) to the 30-min H average measurement (EC), it is expected that modelled H
 508 performs worse than daily ET for the same site and period. Furthermore, for sites with fewer
 509 observations of H (SET 2015 and CGR 2020), especially in the dry season, the metrics showed that
 510 STEAP did not perform as well, for each season, as other sites with more data available. Still, these
 511 limited data were sufficient to show that STEAP outperformed SEBAL in estimating H .



513

514 Fig. 6. Evaluation of observed and modelled: (a) daily evapotranspiration (ET, mm/day) and (b)
 515 instantaneous sensible heat flux (H , at 11:00 am, W/m²) for all experimental sites. STEEP (red
 516 crosses) and SEBAL (black points). The black line is the 1:1 line; the cyan (black) dashed line is
 517 the fitted linear regression between observed and STEEP (SEBAL) model values.

518 We attribute the better performance of STEEP over SEBAL for the Brazilian Caatinga to at
 519 least three reasons, shown in order of impact of model implementation on its performance (Fig. 7
 520 and Table S1). First, by quantifying the remaining λET in the endmembers pixels through the
 521 Priestley-Taylor equation, a more reliable estimate of H in the endmembers pixels can be obtained,
 522 as was also evidenced by Singh and Irmak (2011). This process is critical for the subsequent
 523 numerical calculation of H in SEB models that use dT , as its accuracy is closely related to quantifying
 524 the energy balance at the hot and cold endmembers (Trezza, 2006; Allen et al., 2007; Singh and
 525 Irmak, 2011; Singh et al., 2012). Secondly, roughness characteristics near the surface where the
 526 heat fluxes originate are parameterised by $z0m$, which depends on several factors, such as wind
 527 direction, height and type of the vegetation cover (Kustas et al., 1989b). Estimation of $z0m$ only with
 528 an exponential relationship, as a function of vegetation indices, may be an oversimplification (Kustas
 529 et al., 1989a; Paul et al., 2013). In our study, $z0m$ and $d0$ are calculated with the equations and
 530 coefficients proposed in Raupach (1994) and Verhoef et al. (1997b), and using PAI because this

531 index better represents the intra-annual phenological changes in the Caatinga (Miranda et al., 2020).
 532 This procedure considers the characteristics of SDTF, such as seasonality of phenology and
 533 vegetation height, that considerably affect the quantification of turbulent transfer (Liu et al., 2021).
 534 Third, our study uses the equation described in Verhoef et al. (1997a) and Paul et al. (2013) to
 535 estimate rah , which considers the differences between heat and momentum transfer, unlike the
 536 original equation employed in other SEB models e.g. SEBAL or METRIC that only considers $z0m$
 537 and sets $z0h = 0.1$ when computing this resistance. Furthermore, we account for the kB^{-1} parameter
 538 that varies in space and time and incorporates the soil moisture content obtained by RS (Su et al.,
 539 2001; Gokmen et al., 2012). ET estimation is best represented with a spatially varying kB^{-1} values,
 540 as pointed out by the studies of Gokmen et al. (2012) and Paul et al. (2014). Long et al. (2011) report
 541 that the introduction of these fixed values ($z0h$ or kB^{-1}) has a significant impact on the magnitudes of
 542 the estimates of H. Furthermore, Mallick et al. (2018) and Trebs et al. (2021) indicate that the
 543 parameterization of rah can influence the estimation of ET, especially in SEB models that are largely
 544 dependent on rah . Our results show that including just one or two of the refinements had only partial
 545 performance gains (Fig. 7 and Table S1). In contrast, all the proposed STEEP improvements when
 546 implemented together resulted in the best performance metrics for all sites.

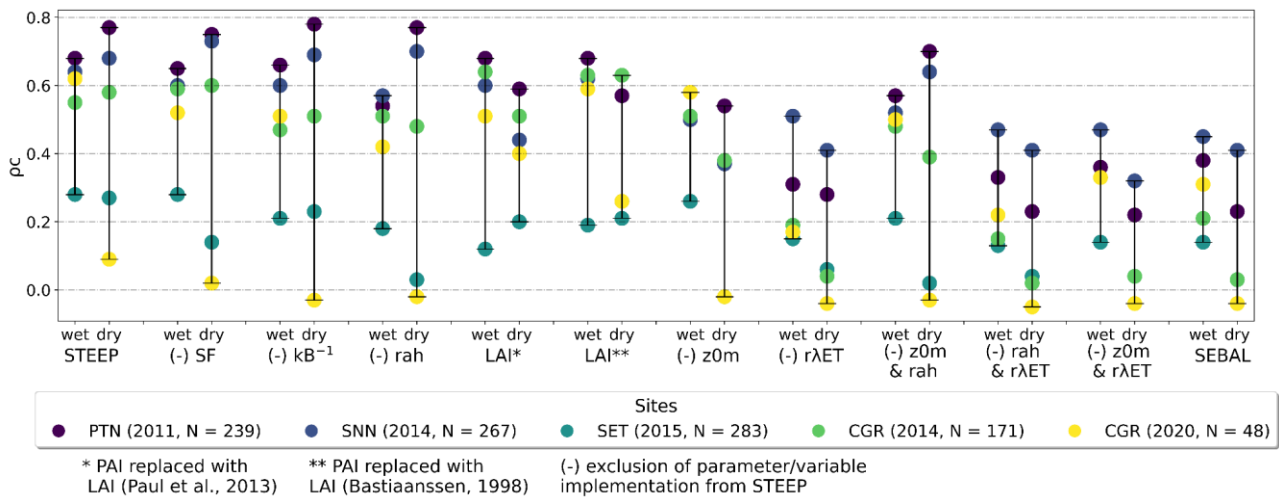
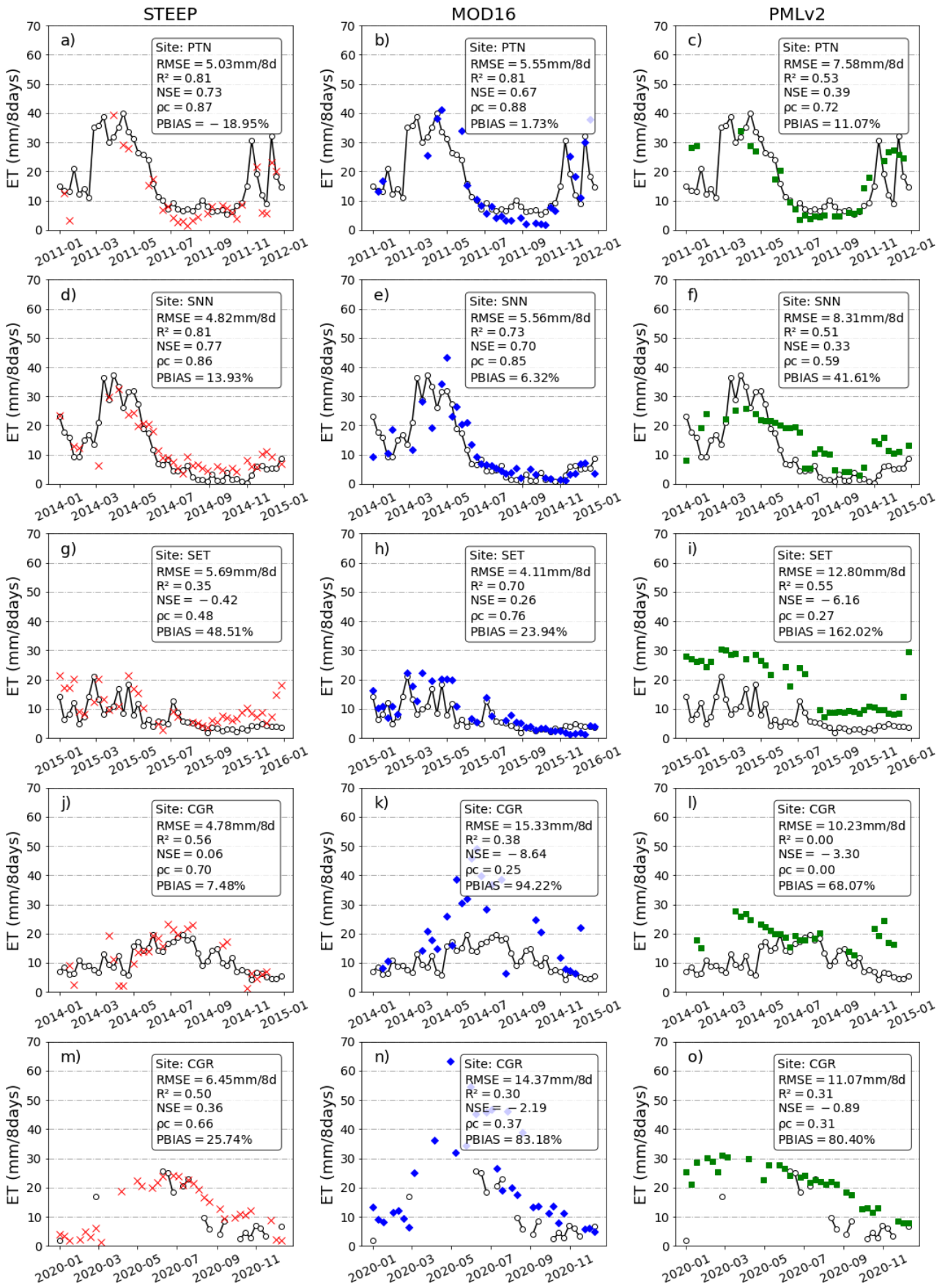


Fig. 7. Change of the concordance correlation coefficient (ρ_c) by the exclusion/modification of one or two parameters/variables implemented in the STEEP model, in the wet and dry seasons: scale factor soil moisture correction (SF), the parameter kB^{-1} , the aerodynamic resistance for heat transfer (rah), PAI replace with LAI (determined by two different methods), the roughness length for momentum transport ($z0m$) and the residual latent heat flux in the end members pixels ($r\lambda ET$).

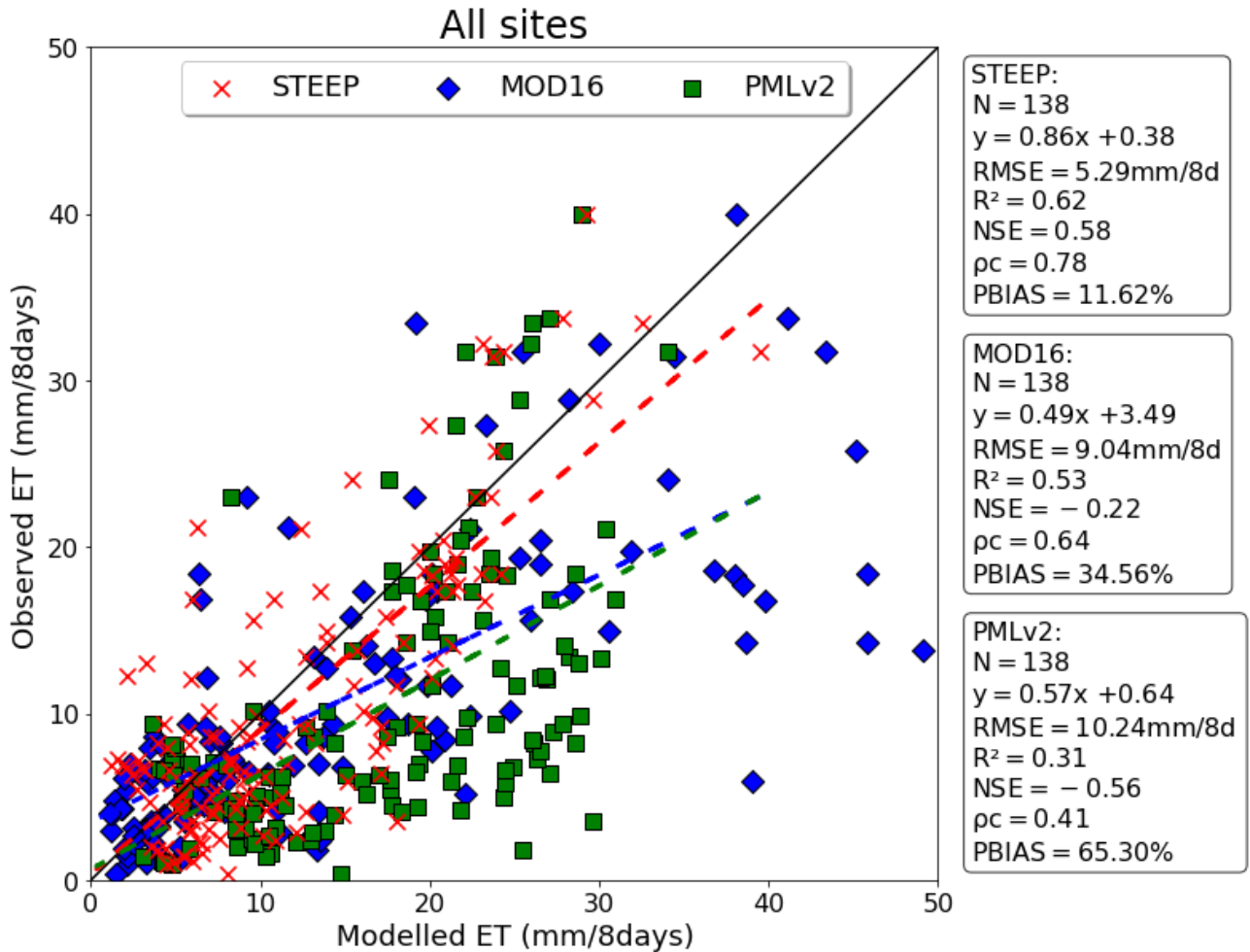
553 3.2 Comparison of STEEP model estimates with global evapotranspiration products

554 The comparison of ET estimates by STEEP, MOD16 and PMLv2 with the observed values
555 at the different sites (Fig. 8) reveals that the ET estimates by STEEP and global products adequately
556 followed the seasonality of the values, with a better fit for STEEP and MOD16. In general, the
557 evaluation at the different sites shows that the *RMSE* of STEEP was not higher than 6.45 mm/8
558 days, while the ET products' maximum *RMSE* was close to 15 mm/8 days. It is noted that the lowest
559 *RMSE* value found (4.11 mm/8 days) was for MOD16 at the SET site. Regarding R^2 values, 80% of
560 the evaluations with STEEP were equal to or greater than 0.50. For MOD16, 60% of the R^2 values
561 were equal to or greater than 0.70, while for PMLv2, no site had R^2 values that exceeded 0.55. The
562 best *NSE* value produced by STEEP was 0.77, while with MOD16, it was 0.70, both at the SNN site,
563 while PMLv2 did not exceed 0.39 (PTN site). Regarding ρ_c , the percentages of ET evaluations that
564 obtained values equal to or greater than 0.70 were 60% for STEEP and MOD16, and only 20% for
565 PMLv2 (site PTN). The overestimations (*PBIAS*) with STEEP were not higher than 50%, and not
566 higher than 95% with MOD16. For PMLv2 the overestimations did not exceed 80%, except for the
567 SET site that obtained a *PBIAS* approx. 160%. We highlight the good performance of MOD16 for
568 the SET, SNN, and especially the PTN sites, with very good performance metrics and seasonal
569 behaviour, capturing ET values in dry periods very well. The evaluation results of STEEP, MOD16
570 and PMLv2 for all observation sites combined are shown in Fig. 9. Noteworthy is the better
571 performance of STEEP over MOD16 and PMLv2, with *RMSE* of < 6 mm/8 days, R^2 and *NSE* greater
572 than or close to 0.60, ρ_c of > 0.75 and an average overestimation < 12%. Analysis with the dataset
573 considering only the 8-day time periods without missing field-observed data, i.e. periods with valid
574 ET measurements during eight consecutive days (Fig. S3) did not change the results overall,
575 confirming STEEP's dominance compared to the two standard products evaluated.

576



578 Fig. 8. Temporal evolution of ET from STEEP, MOD16 and PMLv2 for the different observation
 579 sites, and their individual performance statistics. a), b) and c) PTN 2011; d), e) and f) SNN 2014; g)
 580 h) and i) SET 2015; j), k) and l) CGR 2014; m), n) and o) CGR 2020. Black lines correspond to
 581 observed ET while data points refer to estimates by the STEEP model (red crosses), MOD16 (blue
 582 diamonds) and PMLv2 (green squares) products.



583
 584 Fig. 9. Evaluation of evapotranspiration (ET, mm/8 days) observed and modelled with STEEP (red
 585 crosses), MOD16 (blue diamonds) and PMLv2 (green squares) for all experimental sites. The
 586 black line is the 1:1 line; dashed lines are the fitted linear regressions of observed versus modelled
 587 values by the STEEP model (red), MOD16 (blue) and PMLv2 (green) products. $N = 138$ is the total
 588 number of eight-day periods with at least one day of EC data measured in at least one of the five
 589 experimental sites of Caatinga where all the ET models (STEEP, MOD16 and PMLv2) outputs
 590 were available.

591 The explanation of the differences between STEEP and the MOD16 and PMLv2 products is
592 two-fold. Firstly, the way ET is obtained differs between STEEP and the other products. While
593 STEEP and other SEB single-source models estimate ET as a combined single process, i.e. soil
594 evaporation and transpiration estimates are provided as a lumped sum (Sahnoun et al., 2021), and
595 interception loss is not taken into account, MOD16 and PMLv2 discriminate the ET components, i.e.
596 soil evaporation, transpiration, and wet canopy evaporation (Mu et al., 2011; Zhang et al., 2019).
597 With this in mind it is remarkable that STEEP performs better than the other, widely used, multiple-
598 source ET products. Secondly, the input data sets and their uses are different. The driving
599 meteorological data for STEEP are from ERA5-Land, while in MOD16, they are from MERRA and in
600 PMLv2 are provided by GLDAS (Mu et al., 2011; Zhang et al., 2019). In addition, the meteorological
601 elements used are different among the ET products. MOD16 requires air temperature, atmospheric
602 pressure, relative humidity, and downward shortwave radiation. In addition to these elements,
603 PMLv2 also requires precipitation, downward longwave radiation, and wind speed (Mu et al., 2011;
604 Zhang et al., 2019; Yin et al., 2020; Chen et al., 2022). Although both ET products use the same
605 land cover data (MOD12Q1), only MOD16 integrates it into its algorithm. In MOD16, the land cover
606 type defines biome delimitation for the characterization of leaf stomatal conductance, vapour
607 pressure deficit (VPD) and other related factors, while PMLv2 only uses land cover to construct a
608 mask of the land area (Chen et al., 2022). The sources and use of LAI in these two products are also
609 different. LAI is used to increase leaf conductance in MOD16, while it is used to divide the total
610 available energy into canopy uptake and soil uptake in PMLv2 (Mu et al., 2011; Zhang et al., 2019;
611 Chen et al., 2022). Although MOD16 uses EC data from 46 distributed sites for validation (Mu et al.,
612 2011) and PMLv2 uses EC data from 95 distributed sites and ten plant functional types for calibration
613 (Zhang et al., 2019; Yin et al., 2020), none of the products had observation sites in SDTF.

614 The uncertainties associated with field measurements of ET can also influence the evaluation
615 of the model products. It is generally accepted that EC flux towers provide reliable local, i.e. for areas
616 of relatively limited spatial extensions, ca. 10 km², ET measurements (Mu et al., 2011; Chu et al.,
617 2021; Salazar-Martínez et al., 2022). However, generally flux tower data have a lack of energy
618 balance closure, that is the difference between net radiation and ground heat flux is sometimes
619 greater than the sum of the turbulent latent and sensible heat fluxes, an error that can be in the of

620 10–30% range (Wilson et al., 2002; Foken, 2008; Allen et al., 2011). This gap can result from
621 instrument errors, weather and surface conditions, e.g. those that result in advection, and gap-filling
622 methods (Mu et al., 2011). In addition, the complex and heterogeneous canopy structure, the
623 stochastic nature of turbulence (Hollinger and Richardson, 2005) and adverse weather conditions,
624 e.g. rainy and stormy days, tower sensors recording abnormal values, can affect ET measurements
625 obtained by EC systems (Ramoelo et al., 2014).

626 3.3 Sources of error and further research for STEEP

627 In its current configuration, STEEP has some limitations that should be noted. Meteorological
628 reanalysis provides only large-scale averages and can misrepresent local meteorological conditions;
629 hence, it suffers from biases, especially over heterogeneous surfaces (Rasp et al., 2018). However,
630 despite moderate accuracy and biases at regional scales, ground-based assimilation and reanalysis
631 data have become important sources of meteorological inputs for ET estimates (Mu et al., 2011;
632 Zhang et al., 2019; Allam et al., 2021; Senay et al., 2022). Laipelt et al. (2020) and Kayser et al.
633 (2022) showed that global reanalysis data when used as meteorological inputs had modest effects
634 only on the accuracy of SEBAL for estimating ET. In our study, ERA5-Land exhibited relatively high
635 and satisfactory agreement with micrometeorological data measured at each site (Fig. S4). Also,
636 although gap-filling was used in the present study to improve the availability of LST data, this
637 procedure should be used with caution. In addition, care should be taken when using the MCD43A4
638 reflectance product, because in its composition there is also gap-filling. For example, on some cloudy
639 days, the estimates of vegetation indices, surface albedo, and LST may have introduced
640 inaccuracies in the STEEP (and in SEBAL) model calculation process due to these gap-filling
641 methods. Regarding the selection of endmembers pixels, although the temporal evolution of the
642 selected pixels in this study seems plausible, their representativeness of the actual conditions may
643 be debatable, especially considering the considerable extent of the AOI. The computational capacity
644 and the effectiveness of GEE for running SEB models should be commended. Although other studies
645 have demonstrated GEE's strength (Laipelt et al., 2021; Jaafar et al., 2022; Senay et al., 2022), this
646 platform has some limitations when it comes to the number of iterations, e.g. a convergence
647 threshold cannot be set to stop the within-loop iterations of H calculations; instead a fixed number of

648 iterations needs to be defined. Still, the availability of the several necessary datasets within one
649 platform greatly facilitates the run of STEEP and other SEB models.

650 One of the main focuses of this study is to provide a one-source model capable of
651 representing ET in environments that are mainly governed by soil–water availability, such as those
652 represented by SDTF, in a parsimonious way. Based on our findings we deem this main aim to be
653 achieved due to the relative simplicity of the STEEP model and its low data demand. The improved
654 performance of STEEP was the result of improvement of existing and physically meaningful
655 parameters (z_{0m} and kB^{-1}), rather than by introducing additional empirical parameters, thereby
656 satisfying the principle of equifinality (see Beven and Freer, 2001). To explore further the potential
657 and accuracy of STEEP, more research is needed to analyse the impact that the improved H
658 approach has on ET of different land covers at longer time scales. Despite the promising overall
659 results, additional efforts are required on modelling H in SDTF regions. Although we have shown
660 that STEEP outperforms other models in simulating either H or ET, we acknowledge that there is still
661 room for model improvement. Given that the STEEP model was formulated to be a calibration-free
662 model, it may be possible to improve H estimates by, for example, optimising coefficients associated
663 to soil moisture (see Eq A.12) and applying dynamic values to q_{pt} (see Eq A.25) varying seasonally.
664 Another potential improvement for instantaneous H estimates can be achieved by accounting for
665 biomass heat storage (BHS; Swenson et al., 2019) in STEEP. Meier et al. (2019) have shown that
666 considering BHS can enable land surface models to capture the diurnal asymmetry of the
667 temperature impact on energy fluxes and, consequently, provide improved sub-hourly H . Improving
668 the quantification of regional ET via RS-based SEB models has a great potential to provide a more
669 accurate estimate of the energy and water fluxes in SDTF regions, and will contribute to a better
670 understanding of the water cycle, its uses, and the interrelationships with ecosystem functioning.

671 **4. Conclusions**

672 Our work developed a calibration-free model (STEPP) with an improved approach for
673 estimating the latent and sensible heat fluxes by remote sensing for SDTF. In summary, the main
674 conclusions are:

- 675 • The estimates of H by STEPP allowed ET estimates to be closer to the observed field
676 values than those obtained by SEBAL. Based on all the performance metrics used to

677 analyse the models, STEEP was superior to SEBAL. STEEP showed *RMSE* less than
678 1mm/day, *R*² between 0.24 and 0.69, *NSE* between -0.17 and 0.65, *ρ*_c between 0.41
679 and 0.80 and *PBIAS* between -17% to 54%. Also noteworthy is how well STEEP captured
680 the seasonal course of observed ET.

681 • Compared with ET data from the global MOD16 and PMLv2 products, the STEEP model
682 simulated a similar but generally superior seasonal evolution and its performance metrics
683 were also better. Considering all observation sites simultaneously, at the eight-day scale,
684 STEEP showed superior performance with *RMSE* less than 6 mm/8 days, *R*² and *NSE*
685 equal to or greater than 0.60, *ρ*_c greater than 0.75, and an overestimation of < 12%.

686 Thus, we conclude that STEEP, a one-source model that incorporated the seasonality of the
687 aerodynamic and surface variables, was well-heelled in representing ET in environments that are
688 mainly governed by soil–water availability. All the same, there is a need to evaluate the newly
689 developed STEEP model performance for different land covers, climate, and for longer time series
690 than those considered during the modelling process in this study.

691 **Acknowledgements**

692 The Coordenação de Aperfeiçoamento de Pessoal de Nível Superior-Brazil (CAPES)-Finance Code
693 001, provided scholarships to the first and fifth authors. This work was funded by the Brazilian
694 National Council for Scientific and Technological Development (CNPq), grant 409341/2021-5, by the
695 Paraíba Scientific Foundation (FAPESQ), under grants 010/2021 and 403/2021, and by São Paulo
696 Scientific Foundation (FAPESP), grant 2015/24461-2. CEF is a research unit funded by Fundação
697 para a Ciência e a Tecnologia I.P. (FCT), Portugal (UIDB/00239/2020). MSBM, AV and RLBN
698 acknowledge support by the Newton/NERC/FAPESP Nordeste project (NE/N012526/1 ICL 652 and
699 NE/N012488/1 UoR). RLBN acknowledges support from the European Research Council under the
700 European Union's Horizon 2020 research and innovation programme (grant agreement No: 787203
701 REALM). MSBM thanks to Fundação de Amparo à Ciência e Tecnologia do Estado de Pernambuco
702 (FACEPE) for funding this through the Project FACEPE APQ 0062-1.07/15 (Caatinga-FLUX). MSBM
703 and AMPM acknowledge to the National Observatory of Water and Carbon Dynamics in the Caatinga
704 Biome (INCT: NOWCBCB) supported by FACEPE (grant: APQ-0498-3.07/17 ONDACBC), CNPq
705 (grant: 465764/2014-2), and CAPES (grants: 88887.136369/2017-00).

706 **Data Availability Statement**

707 ET data for the PTN, SNN, and SET sites were published by Melo et al. (2021), and are available at
708 <https://doi.org/10.5281/zenodo.5549321>. ET data for the CGR site; H data for the PTN, SNN, CGR
709 sites, and the code used for the formulation of the STEEP model presented in this study can be
710 accessed at <https://doi.org/10.5281/zenodo.7109043> and
711 https://github.com/ulissesaalencar/ET_SDTF, respectively. H data for the SET site is publicly
712 available for download at <https://ameriflux.lbl.gov/>.

713 **Supplementary material**

714 Table S1. Performance statistics by the exclusion/modification of one or two parameters/variables
715 implemented in the STEEP model, in the wet and dry seasons: scale factor soil moisture correction
716 (SF), the parameter kB^{-1} , the aerodynamic resistance for heat transfer (rah), PAI replace with LAI
717 (determined by two different methods), the roughness length for momentum transport (z_0m), the
718 residual latent heat flux in the end members pixels ($r\lambda ET$), and of the SEBAL model.

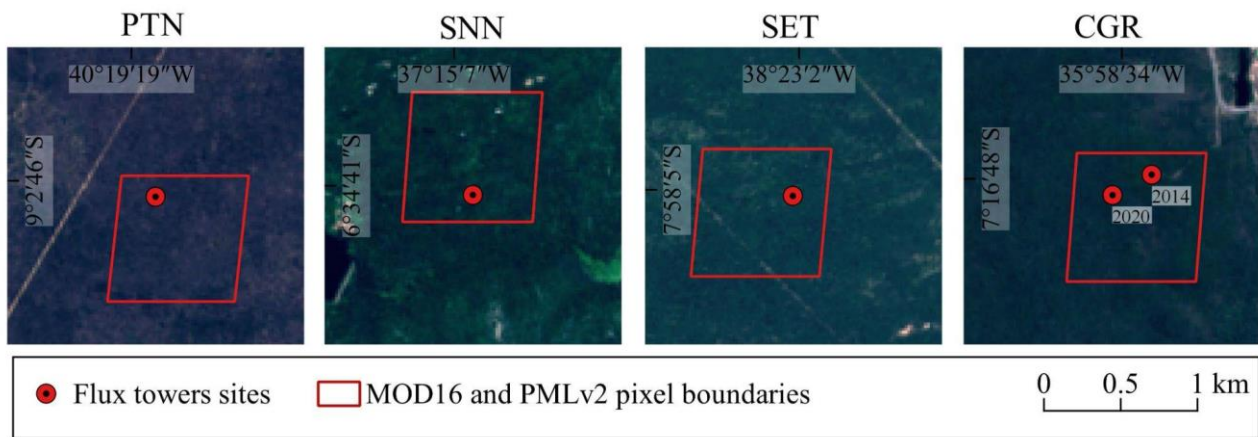
		Performance statistics									
Site		RMSE		R^2		NSE		ρ_c		PBIAS	
		wet	dry	wet	dry	wet	dry	wet	dry	wet	dry
PTN (N = 239; 2011)	STEEP	1.23	0.7	0.53	0.62	0.34	0.5	0.68	0.77	-18.01	-17.01
	(-) SF	1.38	0.69	0.56	0.58	0.16	0.52	0.65	0.75	-26.39	-7.99
	(-) kB-1	1.39	0.67	0.54	0.62	0.14	0.55	0.66	0.78	-23.37	-8.23
	(-) rah	1.61	0.66	0.42	0.6	-0.22	0.55	0.54	0.77	-32.42	-6.56
	LAI*	1.37	1.08	0.57	0.59	0.19	-0.18	0.68	0.59	-24.24	-56.26
	LAI**	1.27	0.91	0.54	0.34	0.28	0.17	0.68	0.57	-19.73	-11.95
	(-) z0m	1.48	0.88	0.36	0.3	0.01	0.21	0.5	0.54	-25.94	7.55
	(-) rλET	1.5	1.6	0.12	0.19	-0.15	-1.54	0.31	0.28	14.75	75.96
	(-) z0m & rah	1.51	0.72	0.44	0.51	-0.04	0.48	0.57	0.7	-28.85	4.4
	(-)rah & rλET	1.47	1.66	0.13	0.15	-0.11	-1.81	0.33	0.23	12.99	81.63
	(-) z0m & rλET	1.42	1.45	0.14	0.09	-0.31	-0.04	0.36	0.22	0.73	57.29
	SEBAL	1.39	1.55	0.16	0.12	0.01	-1.43	0.38	0.23	2.12	69.2
SNN (N = 267; 2014)	STEEP	1.03	0.6	0.46	0.62	0.32	0.25	0.64	0.68	-12.17	58.08
	(-) SF	1.07	0.58	0.47	0.64	0.29	0.44	0.6	0.73	-17.2	42.77
	(-) kB-1	1.12	0.67	0.44	0.59	0.21	0.24	0.6	0.69	-17.86	50.26
	(-) rah	1.19	0.6	0.49	0.62	0.19	0.41	0.57	0.7	-25.47	47.33
	LAI*	1.38	0.8	0.54	0.3	-0.21	-0.07	0.6	0.44	-29.33	-58.36
	LAI**	1.19	0.98	0.52	0.09	0.07	-0.6	0.62	0.26	23.77	55.02
	(-) z0m	1.14	0.83	0.41	0.23	0.24	-0.16	0.5	0.37	-19.01	60.45
	(-) rλET	1.16	1.18	0.32	0.43	0.18	-1.33	0.51	0.41	12.96	122.85
	(-) z0m & rah	1.19	0.63	0.52	0.57	0.17	0.34	0.52	0.64	-26.49	50.69
	(-)rah & rλET	1.13	1.14	0.25	0.37	0.16	-1.19	0.47	0.41	6.43	111.65
	(-) z0m & rλET	1.13	1.03	0.24	0.17	0.16	-0.79	0.47	0.32	-5.86	79.17
	SEBAL	1.13	1.06	0.22	0.33	0.16	-0.88	0.45	0.41	0.91	98.12
SET (N = 283; 2015)	STEEP	1.16	0.6	0.12	0.12	-0.55	-0.94	0.28	0.27	52.19	55.18

	(-) <i>SF</i>	1.04	0.61	0.11	0.02	-0.25	-0.99	0.28	0.14	36.58	38.26
	(-) <i>kB-1</i>	1.13	0.58	0.06	0.07	-0.49	-0.86	0.21	0.23	36.71	40.83
	(-) <i>rah</i>	1.06	0.56	0.04	0	-0.43	-1.03	0.18	0.03	21.82	39.71
	<i>LAI*</i>	1.3	0.68	0.03	0.09	-0.98	-1.51	0.12	0.2	-62.3	-75.32
	<i>LAI**</i>	1.15	0.6	0.04	0.05	-0.53	-0.97	0.19	0.21	-6.83	-29.78
	(-) <i>z0m</i>	1.09	0.75	0.1	0	-0.36	-2.74	0.26	-0.02	42.62	80.96
	(-) <i>rλET</i>	2.11	1.37	0.15	0.04	-4.18	-9.27	0.15	0.06	151.66	190.07
	(-) <i>z0m & rah</i>	1.06	0.58	0.05	0	-0.3	-1.24	0.21	0.02	21.6	51.96
	(-) <i>rah & rλET</i>	1.99	1.37	0.11	0.01	-3.99	-9.27	0.13	0.04	143.27	183.22
	(-) <i>z0m & rλET</i>	1.66	1.16	0.07	0.01	-2.47	-6.31	0.14	0.04	104.32	134.34
	SEBAL	1.83	1.28	0.1	0	-3.21	-7.93	0.14	0.03	128	161.89
	STEEP	0.8	0.72	0.35	0.51	-0.35	-0.8	0.55	0.58	5.85	25.16
CGR (N = 171; 2014)	(-) <i>SF</i>	0.7	0.67	0.36	0.52	-0.02	-0.53	0.59	0.6	6.57	30.14
	(-) <i>kB-1</i>	0.78	0.8	0.25	0.44	-0.28	-1.18	0.47	0.51	15.04	38.9
	(-) <i>rah</i>	0.71	0.78	0.28	0.46	-0.06	-1.07	0.51	0.48	-8.54	54.63
	<i>LAI*</i>	0.76	0.83	0.49	0.61	-0.23	-1.35	0.64	0.51	-7.64	-62.39
	<i>LAI**</i>	0.75	0.68	0.46	0.58	-0.18	-0.57	0.63	0.63	-9.25	-26.31
	(-) <i>z0m</i>	0.71	0.83	0.28	0.35	-0.05	-1.35	0.51	0.38	-11.12	62.72
	(-) <i>rλET</i>	1.15	2.32	0.09	0.07	-1.77	-17.48	0.19	0.04	46.68	217.84
	(-) <i>z0m & rah</i>	0.69	0.84	0.24	0.44	-0.01	-1.43	0.48	0.39	3.9	68.9
	(-) <i>rah & rλET</i>	1.14	2.44	0.05	0.03	-1.72	-19.4	0.15	0.02	43.77	229.58
	(-) <i>z0m & rλET</i>	0.85	1.97	0.11	0.04	-0.51	-12.27	0.33	0.04	9.18	175.39
	SEBAL	0.97	2.24	0.07	0.03	-0.97	-14.7	0.21	0.03	28.63	208.13
	STEEP	0.61	1.06	0.39	0.02	0.29	-2.98	0.62	0.09	-1.19	101.37
	CGR (N = 48; 2020)	(-) <i>SF</i>	0.82	1.03	0.3	0	-0.29	-2.76	0.52	0.02	-6.52
(-) <i>kB-1</i>		0.83	1.26	0.29	0	-0.3	-4.63	0.51	-0.03	-5.31	135.98
(-) <i>rah</i>		1.11	1.13	0.25	0	-1.2	-3.55	0.42	-0.02	-15.37	133.29
<i>LAI*</i>		0.85	1.02	0.29	0.01	-0.38	-0.99	-3.06	0.4	-4.71	31.63
<i>LAI**</i>		0.67	0.76	0.36	0.07	0.14	-1.03	0.59	0.26	-3.58	2.87

(-) $z0m$	0.69	1.03	0.41	0	0.15	-2.73	0.58	-0.02	-12.29	106.1
(-) $r\lambda ET$	0.99	2.25	0.03	0.06	-0.52	-16.98	0.17	-0.04	6.37	312.54
(-) $z0m$ & rah	1.04	1.13	0.34	0.01	-0.74	-3.52	0.5	-0.03	-16.56	134.92
(-) rah & $r\lambda ET$	0.89	2.38	0.05	0.14	-0.24	-19.08	0.22	-0.05	1.07	330.94
(-) $z0m$ & $r\lambda ET$	0.83	1.77	0.18	0.02	-0.6	-10.14	0.33	-0.04	-14.15	216.81
SEBAL	0.81	2.11	0.16	0.07	-0.02	-0.02	0.31	-0.04	-12.25	285.53

720

721 $z0m$ = roughness length for momentum transfer; rah = aerodynamic resistance for heat transfer; $r\lambda ET$ = remaining λET in the endmembers pixels.

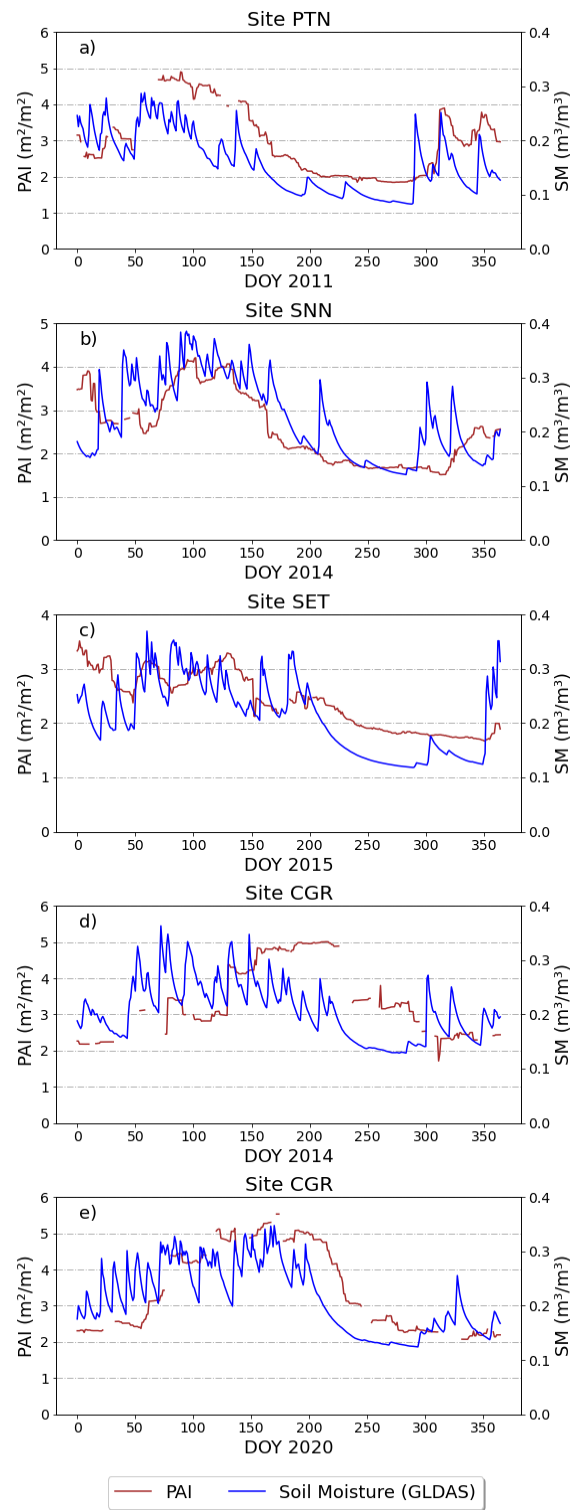


722

723 Fig. S1. Location of the flux towers sites and MOD16 and PMLv2 pixel boundaries. True colour
 724 composite (bands 4, 3, and 2) of Harmonized Sentinel-2 MSI acquired via Google Earth Engine.

725 Scene acquired of PTN (12/06/2021); SNN and SET (25/05/2021); CGR (29/07/2021).

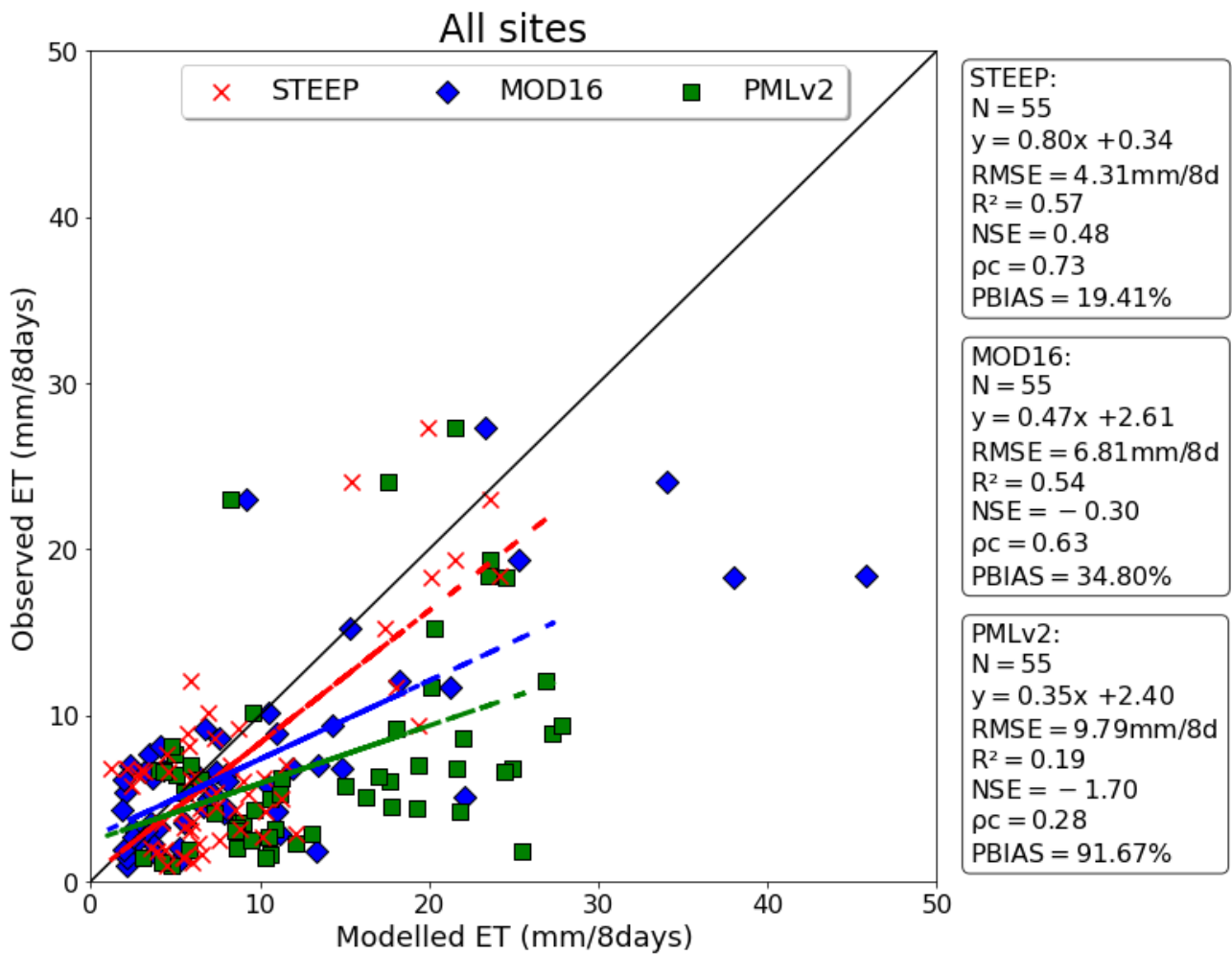
726



727

728

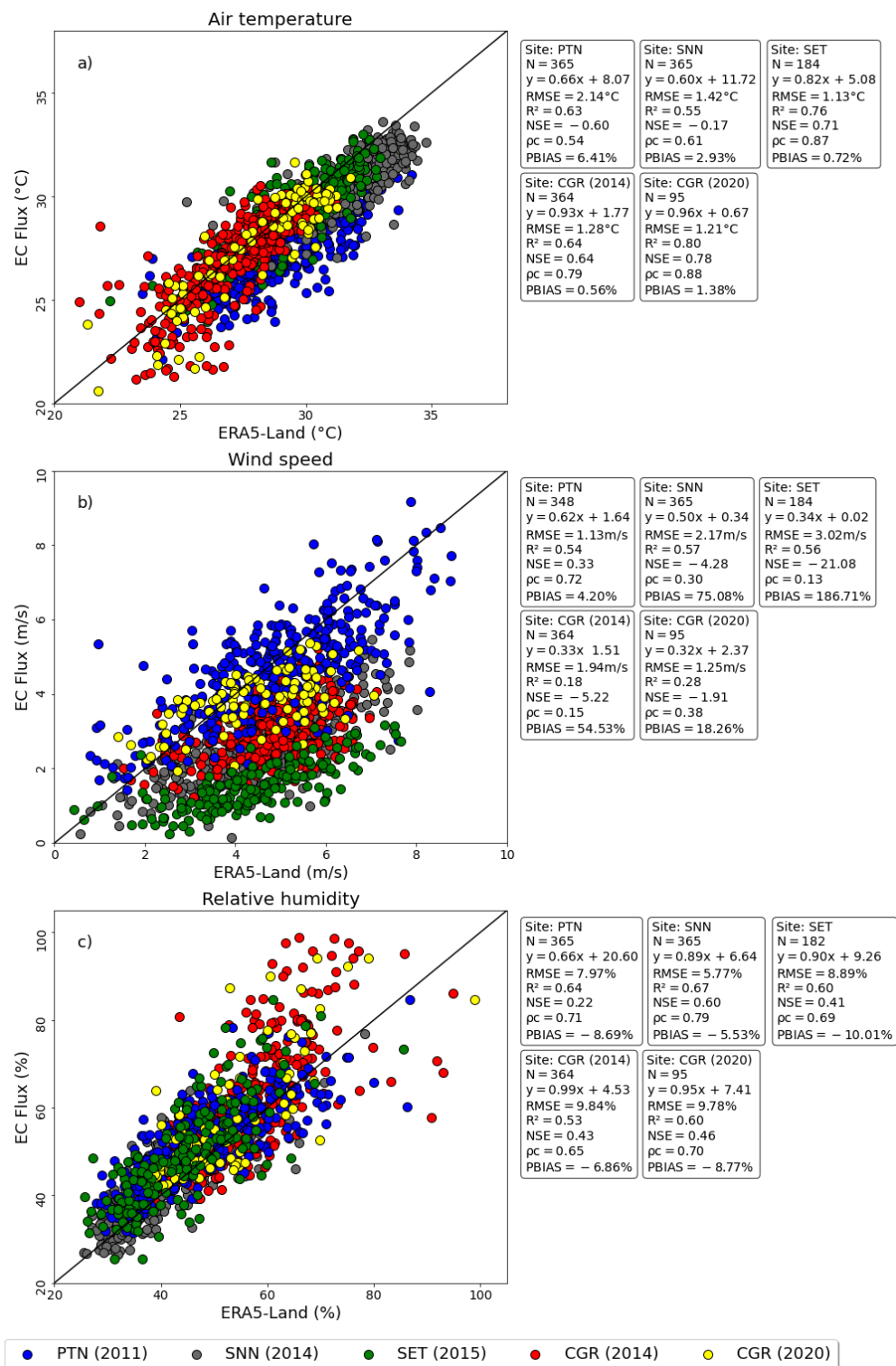
Fig. S2. PAI and soil moisture time series for the different observation sites.



729

730 Fig. S3. Evaluation of evapotranspiration (ET, mm/8 days) observed and modelled with STEEP
 731 (red crosses), MOD16 (blue diamonds) and PMLv2 (green squares) for all experimental sites
 732 considering only the 55 periods where the field-observed data had eight consecutive days. The
 733 black line is the 1:1 line; dashed lines are the fitted linear regressions of observed or modelled
 734 values by the STEEP model (red), MOD16 (blue) and PMLv2 (green) products.

735



736

737

738

739

740

741

742

Fig. S4. Comparison between ERA5-Land reanalysis dataset and local observational meteorological measurements from the flux tower at the closest time from the satellite overpass. Micrometeorological sensors installed at the flux towers are up to 16 m in distance from the land surface, and ERA5-Land variables have different reference elevation (e.g. 2 m for air temperature and 10 m to wind speed).

743 **Appendix A – Equations adopted to formulate the STEEP model**

744 Latent heat flux (λET) was modeled using Eq. (A.1):

$$\lambda ET = R_n - G - H \quad (\text{A.1})$$

745 where R_n is net radiation, G is soil heat flux, and H is sensible heat flux. All variables are expressed
746 in energy units (e.g., W/m^2).

747 Net radiation (R_n) was modeled based on the radiation budget indicated by Allen et al. (2007) and
748 Ferreira et al. (2020) by Eq. (A.2):

$$R_n = R_{S\downarrow} \times (1 - \alpha) + \varepsilon_s \times R_{L\downarrow} - R_{L\uparrow} \quad (\text{A.2})$$

749 where $R_{S\downarrow}$ is incident shortwave radiation (W/m^2) estimated following Allen et al. (2007), α is surface
750 albedo (dimensionless), estimated following Trezza et al. (2013), $R_{L\downarrow}$ is longwave radiation from the
751 atmosphere (W/m^2) estimated following Ferreira et al. (2020) with atmospheric emissivity from
752 Duarte et al. (2006); $R_{L\uparrow}$ is emitted longwave radiation (W/m^2) following Ferreira et al. (2020) with ε_s
753 the surface emissivity (dimensionless), estimated following Long et al. (2010).

754 Soil heat flux (G), expressed as a ratio of net radiation, was estimated following the model by
755 Bastiaanssen et al. (1998):

$$\frac{G}{R_n} = [(LST - 273.15) \times (0.0038 + 0.0074 \times \alpha) \times (1 - 0.98 \times NDVI^4)] \quad (\text{A.3})$$

756 where LST is the surface temperature (K) and NDVI is the Normalized Difference Vegetation Index
757 (dimensionless), estimated following Rouse et al. (1973).

758 Sensible heat flux (H) was modeled using:

$$H = \frac{\rho \times c_p \times dT}{rah} \quad (\text{A.4})$$

759 where ρ is the air density (kg/m^3), c_p refers to the specific heat of air at constant pressure ($\text{J}/\text{kg}/\text{K}$),
760 dT is the temperature gradient (K), and rah is the aerodynamic resistance for heat transfer (s/m).

761

762 Aerodynamic resistance to heat transport was estimated based on the classical equation given in
763 Paul et al. (2013), see also Verhoef et al. (1997a):

$$rah = \frac{1}{k \times u^*} \times \left[\ln \left(\frac{z_{ref} - d0}{z0m} \right) - \psi_h \right] + \frac{1}{k \times u^*} \times kB_{umd}^{-1} \quad (A.5)$$

764 where k is the von Kármán constant taken as 0.41, u^* is the friction velocity (m/s), z_{ref} is the
 765 reference height (m), $d0$ is zero plane displacement height (m), $z0m$ is roughness length for
 766 momentum transfer (m), ψ_h is the atmospheric stability correction function for heat transfer (m), as
 767 calculated following Paulson (1970), kB_{umd}^{-1} is the dimensionless parameter formulated to express
 768 the excess resistance of heat transfer compared to momentum transfer, corrected for soil moisture
 769 derived from remote sensing.

770 The friction velocity was computed according to Verhoef et al. (1997b) and Paul et al. (2013):

$$u^* = k \times u \left[\ln \left(\frac{z_{ref} - d0}{z0m} \right) - \psi_m \right]^{-1} \quad (A.6)$$

771 where u is the wind speed (m/s) at a known height z_{ref} , ψ_m is the atmospheric stability correction
 772 function for momentum transfer (m), as calculated following Paulson (1970).

773 Roughness length for momentum transport was estimated, based on the studies by Verhoef et al.
 774 (1997b):

$$z0m = (HGHT - d0) \times \exp(-k \times \gamma + PSICORR) \quad (A.7)$$

775 where $HGHT$ is the height of the vegetation (m), $PSICORR$ is taken as 0.2 and γ is the inverse of the
 776 square root of the bulk surface drag coefficient at the roughness canopy height (Raupach, 1992).

777 Zero plane displacement height ($d0$) was obtained following Raupach (1994) from:

$$d0 = HGHT \times \left[\left(1 - \frac{1}{\sqrt{CD1 \times PAI}} \right) + \left(\frac{\exp^{-\sqrt{CD1 \times PAI}}}{\sqrt{CD1 \times PAI}} \right) \right] \quad (A.8)$$

778 where $CD1$ is taken as 20.6 and PAI is the Plant Area Index.

779 γ was following Verhoef et al. (1997b):

$$\gamma = \left(CD + CR \times \frac{PAI}{2} \right)^{-0.5} \quad (A.9)$$

780 if $\gamma < 3.33$, γ is set to 3.33. Following Verhoef et al. (1997), CD and CR are taken as 0.01 and 0.35,
 781 respectively.

782 Plant Area Index was calculated according to Miranda et al. (2020) as:

$$PAI = 10.1 \times (\rho_{NIR} - \sqrt{\rho_{RED}}) + 3.1 \quad (A.10)$$

783 where ρ_{NIR} is the near infrared band reflectance, and ρ_{RED} is the red band reflectance. If $PAI < 0$, $d0$
 784 is set to 0.

785 The dimensionless parameter kB_{umd}^{-1} is corrected by soil moisture by remote sensing following the
 786 equations provided by Gokmen et al. (2012):

$$kB_{umd}^{-1} = SF \times kB^{-1} \quad (A.11)$$

787 where SF is a scaling factor, represented by a sigmoid function:

$$SF = \left[c + \frac{1}{1 + \exp(d - e \times SM_{rel})} \right] \quad (A.12)$$

788 Here, c , d , e are the sigmoid function coefficients, for which we adopted values of 0.3, 2.5, and 4,
 789 respectively, following Gokmen et al. (2012). SM_{rel} is the relative soil moisture, obtained from:

$$SM_{rel} = \frac{SM - SM_{min}}{SM_{max} - SM_{min}} \quad (A.13)$$

790 where SM is the actual soil moisture content, in our case obtained with the GLDAS reanalysis
 791 product, and SM_{min} and SM_{max} are the minimum and maximum soil moisture. The SM_{min} and SM_{max}
 792 values were obtained using the annual time series analysis of the soil moisture data.

793 kB^{-1} was calculated according to Su et al. (2001):

$$kB^{-1} = \frac{k \times Cd}{4 \times Ct \times \frac{u^*}{u(h)} \times \left(1 - \exp\left(\frac{-nec}{2}\right) \right)} \times f_c^2 + \frac{k \times \frac{u^*}{u(h)} \times \frac{z0m}{h}}{C_t^*} \times f_c^2 \times f_s^2 + kB_s^{-1} \times f_s^2 \quad (A.14)$$

794 where $kB_s^{-1} = 2.46(Re^*)^{0.25} - 2$, Cd is the drag coefficient of the foliage elements taken as 0.2, Ct
 795 is the heat transfer coefficient of the leaf with value 0.01.

796 The ratio $\frac{u^*}{u(h)}$ is parameterized as:

$$\frac{u^*}{u(h)} = c1 - c2 \times \exp(-c3 \times Cd \times PAI) \quad (A.15)$$

797 where $c1 = 0.320$, $c2 = 0.264$, $c3 = 15.1$.

798 nec is the extinction coefficient of the wind speed profile within the canopy given by:

$$nec = \frac{Cd \times PAI}{\frac{2u^{*2}}{u(h)^2}} \quad (A.16)$$

799 C_t^* is heat transfer coefficient of the soil given by:

$$C_t^* = Pr^{-2/3} \times (Re)^{-1/2} \quad (A.17)$$

800 where Pr is the Prandtl number with a value 0.71, and Re is the Reynolds number calculated as:

$$Re = \frac{u^* \times 0.009}{\nu}, \quad \nu = 1.461 \times 10^{-5} \quad (A.18)$$

801 where ν is the kinematic viscosity (m^2/s).

802 In Eq. A.14 f_c is the fractional canopy cover calculated according to Eq. (A19), and f_s is its
803 complement.

$$f_c = 1 - \left[\frac{NDVI - NDVI_{max}}{NDVI_{min} - NDVI_{max}} \right]^{0.4631} \quad (A.19)$$

804 where $NDVI_{max}$ and $NDVI_{min}$ are maximum and minimum NDVI values, respectively. $NDVI_{max}$ and
805 $NDVI_{min}$ values were obtained using the annual time series analysis of the NDVI.

806 dT in Eq. (A4) was estimated daily with a linear relationship on the surface temperature
807 (Bastiaanssen et al., 1998) as:

$$dT = a + b \times LST \quad (A.20)$$

808 To find the coefficients a and b in Eq. (A20) requires that hot and cold endmembers pixels are
809 established. The coefficients were found as:

$$b = \frac{(dT_{hot} - dT_{cold})}{(LST_{hot} - LST_{cold})} \quad (A.21)$$

$$a = dT_{cold} - b \times LST_{cold} \quad (A.22)$$

$$dT_{hot/cold} = \frac{H_{hot/cold} \times rah_{hot/cold}}{\rho \times c_p} \quad (A.23)$$

$$H_{hot/cold} = Rn_{hot/cold} - G_{hot/cold} - \lambda ET_{hot/cold} \quad (A.24)$$

810 where $dT_{hot/cold}$ are dT values for the hot/dry and cold/wet endmember pixels, respectively,
 811 $Rn_{hot/cold}$, $G_{hot/cold}$, $LST_{hot/cold}$, $rah_{hot/cold}$ are the median values extracted on the endmember
 812 pixels of each variable. The selection of endmember pixels is detailed in section 2.3.

813 $\lambda ET_{hot/cold}$ is the term incorporated in the computation of H in the endmember pixels given by the
 814 Priestley-Taylor (1972) equation, according to Singh and Irmak (2011) and French et al. (2015):

$$\lambda ET_{hot/cold} = (Rn_{hot/cold} - G_{hot/cold}) \times f_c \times \alpha_{pt} \times \left[\frac{\Delta}{\Delta + \gamma_c} \right] \quad (A.25)$$

815 where α_{pt} is the empirical Priestley-Taylor coefficient, nominally set to 1.26, but here adjusted
 816 according to local conditions, i.e. we adopted the α_{pt} values (0.55 for hot/dry and 1.75 for cold/wet
 817 pixels) based on Ai and Yang (2016). Δ is the slope of the saturation vapor pressure-air temperature
 818 curve (kPa/°C) and γ_c is the psychrometric constant (kPa/°C).

819 The actual daily evapotranspiration (mm/day) was obtained by means of the following relationship:

$$ET_{24h} = \frac{86400}{(2.501 - 0.00236 \times T_a) \times 10^6} \times \frac{\lambda ET}{Rn - G} \times Rn_{24h} \quad (A.26)$$

820 where T_a is the mean daily air temperature (°C), λET is derived from Eq. A1, and Rn_{24h} corresponds
 821 to the daily net radiation (W/m²); in this study both driving variables were obtained with data from the
 822 ERA5-Land product.

823 **References**

- 824 Ai, Z., & Yang, Y. (2016). Modification and Validation of Priestley–Taylor Model for Estimating Cotton
 825 Evapotranspiration under Plastic Mulch Condition. *Journal of Hydrometeorology*, 17(4), 1281–1293.
 826 doi:10.1175/jhm-d-15-0151.1
- 827 Akoglu, H. (2018). User's guide to correlation coefficients. *Turkish Journal of Emergency Medicine*,
 828 18(3), 91-93. doi: 10.1016/j.tjem.2018.08.001
- 829 Alberton, B., Torres, R. da S., Cancian, L. F., Borges, B. D., Almeida, J., Mariano, G. C., ... Morellato,
 830 L. P. C. (2017). Introducing digital cameras to monitor plant phenology in the tropics: applications for
 831 conservation. *Perspectives in Ecology and Conservation*, 15(2), 82–90.
 832 doi:10.1016/j.pecon.2017.06.004

833 Allam, M., Mhaweji, M., Meng, Q., Faour, G., Abunnasr, Y., Fadel, A., & Xinli, H. (2021). Monthly 10-
834 m evapotranspiration rates retrieved by SEBALI with Sentinel-2 and MODIS LST data. *Agricultural*
835 *Water Management*, 243, 106432. doi:10.1016/j.agwat.2020.106432

836 Allen, R. G., Tasumi, M., & Trezza, R. (2007). Satellite-Based Energy Balance for Mapping
837 Evapotranspiration with Internalized Calibration (METRIC)—Model. *Journal of Irrigation and*
838 *Drainage Engineering*, 133(4), 380–394. doi:10.1061/(asce)0733-9437(2007)133:4(380)

839 Allen, K., Dupuy, J. M., Gei, M. G., Hulshof, C., Medvigy, D., Pizano, C., ... Powers, J. S. (2017).
840 Will seasonally dry tropical forests be sensitive or resistant to future changes in rainfall regimes?
841 *Environmental Research Letters*, 12(2), 023001. doi:10.1088/1748-9326/aa5968

842 Allen, R. G., Pereira, L. S., Howell, T. A., & Jensen, M. E. (2011). Evapotranspiration information
843 reporting: I. Factors governing measurement accuracy. *Agricultural Water Management*, 98(6), 899–
844 920. doi:10.1016/j.agwat.2010.12.015

845 Alvares, C. A., Stape, J. L., Sentelhas, P. C., Gonçalves, J. D. M., & Sparovek, G. (2013). Köppen's
846 climate classification map for Brazil. *Meteorologische Zeitschrift*, 22(6), 711-728. doi:10.1127/0941-
847 2948/2013/0507

848 Anapalli, S. S., Ahuja, L. R., Gowda, P. H., Ma, L., Marek, G., Evett, S. R., & Howell, T. A. (2016).
849 Simulation of crop evapotranspiration and crop coefficients with data in weighing lysimeters.
850 *Agricultural Water Management*, 177, 274–283. doi:10.1016/j.agwat.2016.08.009

851 Anderson, M. C., Kustas, W. P., Norman, J. M., Hain, C. R., Mecikalski, J. R., Schultz, L., ... Gao,
852 F. (2011). Mapping daily evapotranspiration at field to continental scales using geostationary and
853 polar orbiting satellite imagery. *Hydrology and Earth System Sciences*, 15(1), 223–239.
854 doi:10.5194/hess-15-223-2011

855 Andrade, J., Cunha, J., Silva, J., Rufino, I., & Galvão, C. (2021). Evaluating single and multi-date
856 Landsat classifications of land-cover in a seasonally dry tropical forest. *Remote Sensing*
857 *Applications: Society and Environment*, 22, 100515. doi:10.1016/j.rsase.2021.100515

858 Antonino, A. C. D. (2019), AmeriFlux BASE BR-CST Caatinga Serra Talhada, Ver. 1-5, AmeriFlux
859 AMP, (Dataset). <https://doi.org/10.17190/AMF/1562386>

860 Araújo, J. C., & González Piedra, J. I. (2009). Comparative hydrology: analysis of a semiarid and a
861 humid tropical watershed. *Hydrological Processes*, 23(8), 1169–1178. doi:10.1002/hyp.7232

862 Barbosa, H. A., Huete, A. R., & Baethgen, W. E. (2006). A 20-year study of NDVI variability over the
863 Northeast Region of Brazil. *Journal of Arid Environments*, 67(2), 288–307.
864 doi:10.1016/j.jaridenv.2006.02.022

865 Barbosa, A. D. S., Andrade, A. P. de, Félix, L. P., Aquino, Í. D. S., & Silva, J. H. C. S. (2020).
866 Composição, similaridade e estrutura do componente arbustivo-arbóreo de áreas de Caatinga.
867 *Nativa*, 8(3), 314–322. doi:10.31413/nativa.v8i3.9494

868 Barraza, V., Restrepo-Coupe, N., Huete, A., Grings, F., Beringer, J., Cleverly, J., & Eamus, D.
869 (2017). Estimation of latent heat flux over savannah vegetation across the North Australian Tropical
870 Transect from multiple sensors and global meteorological data. *Agricultural and Forest Meteorology*,
871 232, 689-703. doi:10.1016/j.agrformet.2016.10.013

872 Bastiaanssen, W. G. M. (1995). Regionalization of surface flux densities and moisture indicators in
873 composite terrain: A remote sensing approach under clear skies in Mediterranean climates.
874 Wageningen University and Research.

875 Bastiaanssen, W. G. M., Menenti, M., Feddes, R. A., & Holtslag, A. A. M. (1998). A remote sensing
876 surface energy balance algorithm for land (SEBAL). 1. Formulation. *Journal of Hydrology*, 212-213,
877 198–212. doi:10.1016/s0022-1694(98)00253-4

878 Bastiaanssen, W. G. M., Ahmad, M.-D., & Chemin, Y. (2002). Satellite surveillance of evaporative
879 depletion across the Indus Basin. *Water Resources Research*, 38(12), 9–1–9–9.
880 doi:10.1029/2001wr000386

881 Bastiaanssen, W. G. M., Noordman, E. J. M., Pelgrum, H., Davids, G., Thoreson, B. P., & Allen, R.
882 G. (2005). SEBAL Model with remotely sensed data to improve water-resources management under

883 actual field conditions. *Journal of Irrigation and Drainage Engineering*, 131(1), 85–93.
884 doi:10.1061/(asce)0733-9437(2005)131:1(85)

885 Beven, K., & Freer, J. (2001). Equifinality, data assimilation, and uncertainty estimation in
886 mechanistic modelling of complex environmental systems using the GLUE methodology. *Journal of*
887 *Hydrology*, 249(1–4), 11–29. doi:10.1016/s0022-1694(01)00421-8

888 Bhattarai, N., Quackenbush, L. J., Im, J., & Shaw, S. B. (2017). A new optimized algorithm for
889 automating endmember pixel selection in the SEBAL and METRIC models. *Remote Sensing of*
890 *Environment*, 196, 178–192. doi:10.1016/j.rse.2017.05.009.

891 Bonan, G. B., Patton, E. G., Finnigan, J. J., Baldocchi, D. D., & Harman, I. N. (2021). Moving beyond
892 the incorrect but useful paradigm: reevaluating big-leaf and multilayer plant canopies to model
893 biosphere-atmosphere fluxes – a review. *Agricultural and Forest Meteorology*, 306, 108435.
894 <https://doi.org/10.1016/j.agrformet.2021.108435>

895 Borges, C. K., dos Santos, C. A. C., Carneiro, R. G., da Silva, L. L., de Oliveira, G., Mariano, D., ...
896 de S. Medeiros, S. (2020). Seasonal variation of surface radiation and energy balances over two
897 contrasting areas of the seasonally dry tropical forest (Caatinga) in the Brazilian semi-arid.
898 *Environmental Monitoring and Assessment*, 192(8). doi:10.1007/s10661-020-08484-y

899 Brazil, Ministério do Meio Ambiente. Caatinga. <https://antigo.mma.gov.br/biomas/caatinga.html>.
900 Accessed: 25 March 2021.

901 Cabral, O. M. R., Freitas, H. C., Cuadra, S. V., de Andrade, C. A., Ramos, N. P., Grutzmacher, P.,
902 ... Rossi, P. (2020). The sustainability of a sugarcane plantation in Brazil assessed by the eddy
903 covariance fluxes of greenhouse gases. *Agricultural and Forest Meteorology*, 282-283, 107864.
904 doi:10.1016/j.agrformet.2019.107864

905 Campos, S., Mendes, K. R., da Silva, L. L., Mutti, P. R., Medeiros, S. S., Amorim, L. B., ... Bezerra,
906 B. G. (2019). Closure and partitioning of the energy balance in a preserved area of a Brazilian

907 seasonally dry tropical forest. *Agricultural and Forest Meteorology*, 271, 398–412.
908 doi:10.1016/j.agrformet.2019.03.018

909 Carvalho, H. F. D. S., de Moura, M. S., da Silva, T. G., & Rodrigues, C. T. (2018). Controlling factors
910 of 'Caatinga' and sugarcane evapotranspiration in the Sub-middle São Francisco Valley. *Revista*
911 *Brasileira de Engenharia Agrícola e Ambiental*, 22, 225-230. doi:10.1590/1807-
912 1929/agriambi.v22n4p225-230

913 Chai, T., & Draxler, R. R. (2014). Root mean square error (RMSE) or mean absolute error (MAE)?
914 – Arguments against avoiding RMSE in the literature. *Geoscientific Model Development*, 7(3), 1247–
915 1250. doi:10.5194/gmd-7-1247-2014

916 Chehbouni, A., Seen, D. L., Njoku, E. G., & Monteny, B. M. (1996). Examination of the difference
917 between radiative and aerodynamic surface temperatures over sparsely vegetated surfaces. *Remote*
918 *Sensing of Environment*, 58(2), 177-186. doi: 10.1016/S0034-4257(96)00037-5

919 Chen, J. M., & Liu, J. (2020). Evolution of evapotranspiration models using thermal and shortwave
920 remote sensing data. *Remote Sensing of Environment*, 237, 111594. doi:10.1016/j.rse.2019.111594

921 Chen, H., Gnanamoorthy, P., Chen, Y., Mansaray, L. R., Song, Q., Liao, K., ... Sun, C. (2022).
922 Assessment and Inter-Comparison of Multi-Source High Spatial Resolution Evapotranspiration
923 Products over Lancang–Mekong River Basin, Southeast Asia. *Remote Sensing*, 14(3), 479.
924 doi:10.3390/rs14030479

925 Cheng, M., Jiao, X., Li, B., Yu, X., Shao, M., & Jin, X. (2021). Long time series of daily
926 evapotranspiration in China based on the SEBAL model and multisource images and validation.
927 *Earth System Science Data*, 13(8), 3995–4017. doi:10.5194/essd-13-3995-2021

928 Chu, H., et al. (2021) Representativeness of Eddy-Covariance flux footprints for areas surrounding
929 AmeriFlux sites." *Agricultural and Forest Meteorology* 301-302, 108350.
930 doi:org/10.1016/j.agrformet.2021.108350

931 Costa, J. A.; Navarro-Hevia, J., Costa, C. A. G., & de Araújo, J. C. (2021). Temporal dynamics of
932 evapotranspiration in semiarid native forests in Brazil and Spain using remote sensing. *Hydrological*
933 *Processes*, 35(3). doi:10.1002/hyp.14070

934 Costa-Filho, E., Chávez, J. L., Zhang, H., & Andales, A. A. (2021). An optimized surface aerodynamic
935 temperature approach to estimate maize sensible heat flux and evapotranspiration. *Agricultural and*
936 *Forest Meteorology*, 311, 108683. doi:10.1016/j.agrformet.2021.108683

937 Cunha, J., Nóbrega, R. L. B., Rufino, I., Erasmi, S., Galvão, C., & Valente, F. (2020). Surface albedo
938 as a proxy for land-cover clearing in seasonally dry forests: Evidence from the Brazilian Caatinga.
939 *Remote Sensing of Environment*, 238, 111250. doi:10.1016/j.rse.2019.111250

940 Danelichen, V. H. de M., Biudes, M. S., Souza, M. C., Machado, N. G., Silva, B. B. da, & Nogueira,
941 J. de S. (2014). Estimation of soil heat flux in a neotropical Wetland region using remote sensing
942 techniques. *Revista Brasileira de Meteorologia*, 29(4), 469–482. doi:10.1590/0102-778620120568

943 Dombroski, J. L. D., Praxedes, S. C., de Freitas, R. M. O., & Pontes, F. M. (2011). Water relations
944 of Caatinga trees in the dry season. *South African Journal of Botany*, 77(2), 430–434.
945 doi:10.1016/j.sajb.2010.11.001

946 Duarte, H. F., Dias, N. L., & Maggiotto, S. R. (2006). Assessing daytime downward longwave
947 radiation estimates for clear and cloudy skies in Southern Brazil. *Agricultural and Forest*
948 *Meteorology*, 139(3–4), 171–181. doi:10.1016/j.agrformet.2006.06.008

949 Faivre, R., Colin, J., & Menenti, M. (2017). Evaluation of Methods for Aerodynamic Roughness
950 Length Retrieval from Very High-Resolution Imaging LIDAR Observations over the Heihe Basin in
951 China. *Remote Sensing*, 9(1), 63. doi:10.3390/rs9010063

952 Farr, T. G., Rosen, P. A., Caro, E., Crippen, R., Duren, R., Hensley, S., ... & Alsdorf, D. (2007). The
953 shuttle radar topography mission. *Reviews of geophysics*, 45(2). doi:10.1029/2005RG000183

954 Ferreira, T. R., Silva, B. B. D., Moura, M. S. B. D., Verhoef, A., & Nóbrega, R. L. B. (2020). The use
955 of remote sensing for reliable estimation of net radiation and its components: a case study for

956 contrasting land covers in an agricultural hotspot of the Brazilian semiarid region. *Agricultural and*
957 *Forest Meteorology*, 291, 108052. doi:10.1016/j.agrformet.2020.108052

958 Foken, T. (2008). The energy balance closure problem: An overview. *Ecological Applications*, 18(6),
959 1351-1367. doi:10.1890/06-0922.1

960 French, A. N., Hunsaker, D. J., & Thorp, K. R. (2015). Remote sensing of evapotranspiration over
961 cotton using the TSEB and METRIC energy balance models. *Remote Sensing of Environment*, 158,
962 281–294. doi:10.1016/j.rse.2014.11.003

963 Funk, C., Peterson, P., Landsfeld, M., Pedreros, D., Verdin, J., Shukla, S., ... & Michaelsen, J. (2015).
964 The climate hazards infrared precipitation with stations—a new environmental record for monitoring
965 extremes. *Scientific data*, 2(1), 1-21. doi:10.1038/sdata.2015.66

966 Gan, R., Zhang, Y., Shi, H., Yang, Y., Eamus, D., Cheng, L., ... Yu, Q. (2018). Use of satellite leaf
967 area index estimating evapotranspiration and gross assimilation for Australian ecosystems.
968 *Ecohydrology*, 11(5), e1974. doi:10.1002/eco.1974

969 Gokmen, M., Vekerdy, Z., Verhoef, A., Verhoef, W., Batelaan, O., & van der Tol, C. (2012).
970 Integration of soil moisture in SEBS for improving evapotranspiration estimation under water stress
971 conditions. *Remote Sensing of Environment*, 121, 261–274. doi:10.1016/j.rse.2012.02.003

972 Gorelick, N., Hancher, M., Dixon, M., Ilyushchenko, S., Thau, D., & Moore, R. (2017). Google Earth
973 Engine: Planetary-scale geospatial analysis for everyone. *Remote Sensing of Environment*, 202,
974 18–27. doi:10.1016/j.rse.2017.06.031

975 Gupta, H. V., Sorooshian, S., & Yapo, P. O. (1999). Status of automatic calibration for hydrologic
976 models: Comparison with multilevel expert calibration. *Journal of hydrologic engineering*, 4(2), 135-
977 143. doi:10.1061/(ASCE)1084-0699(1999)4:2(135)

978 Hallak, R. & Pereira Filho, A. J. (2011). Metodologia para análise de desempenho de simulações de
979 sistemas convectivos na região metropolitana de São Paulo com o modelo ARPS: sensibilidade a

980 variações com os esquemas de advecção e assimilação de dados. *Revista Brasileira de*
981 *Meteorologia*, 26, 591-608. doi:10.1590/S0102-77862011000400009

982 Hollinger, D. Y., & Richardson, A. D. (2005). Uncertainty in eddy covariance measurements and its
983 application to physiological models. *Tree Physiology*, 25(7), 873–885.
984 doi:10.1093/treephys/25.7.873

985 Jaafar, H., Mourad, R., & Schull, M. (2022). A global 30-m ET model (HSEB) using harmonized
986 Landsat and Sentinel-2, MODIS and VIIRS: Comparison to ECOSTRESS ET and LST. *Remote*
987 *Sensing of Environment*, 274, 112995. doi:10.1016/j.rse.2022.112995

988 Jia, L., Su, Z., van den Hurk, B., Menenti, M., Moene, A., De Bruin, H. A. ., ... Cuesta, A. (2003).
989 Estimation of sensible heat flux using the Surface Energy Balance System (SEBS) and ATSR
990 measurements. *Physics and Chemistry of the Earth, Parts A/B/C*, 28(1-3), 75–88.
991 doi:10.1016/s1474-7065(03)00009-3

992 Kayser, R. H., Ruhoff, A., Laipelt, L., de Mello Kich, E., Roberti, D. R., de Arruda Souza, V., ... &
993 Neale, C. M. U. (2022). Assessing geeSEBAL automated calibration and meteorological reanalysis
994 uncertainties to estimate evapotranspiration in subtropical humid climates. *Agricultural and Forest*
995 *Meteorology*, 314, 108775. doi:10.1016/j.agrformet.2021.108775

996 Koch, R., Almeida-Cortez, J. S., & Kleinschmit, B. (2017). Revealing areas of high nature
997 conservation importance in a seasonally dry tropical forest in Brazil: Combination of modelled plant
998 diversity hot spots and threat patterns. *Journal for Nature Conservation*, 35, 24–39.
999 doi:10.1016/j.jnc.2016.11.004

1000 Kustas, W., Choudhury, B. Moran, M., Reginato, R., Jackson, R., Gay, L., & Weaver, H. (1989a).
1001 Determination of sensible heat flux over sparse canopy using thermal infrared data. *Agricultural and*
1002 *Forest Meteorology*, 44(3-4), 197–216. doi:10.1016/0168-1923(89)90017-8

- 1003 Kustas, W. P., Choudhury, B. J., Kunkel, K. E., & Gay, L. W. (1989b). Estimate of the aerodynamic
1004 roughness parameters over an incomplete canopy cover of cotton. *Agricultural and Forest*
1005 *Meteorology*, 46(1-2), 91-105. doi:10.1016/0168-1923(89)90114-7
- 1006 Laipelt, L., Ruhoff, A. L., Fleischmann, A. S., Kayser, R. H. B., Kich, E. de M., da Rocha, H. R., &
1007 Neale, C. M. U. (2020). Assessment of an Automated Calibration of the SEBAL Algorithm to Estimate
1008 Dry-Season Surface-Energy Partitioning in a Forest–Savanna Transition in Brazil. *Remote Sensing*,
1009 12(7), 1108. doi:10.3390/rs12071108
- 1010 Laipelt, L., Henrique Bloedow Kayser, R., Santos Fleischmann, A., Ruhoff, A., Bastiaanssen, W.,
1011 Erickson, T. A., & Melton, F. (2021). Long-term monitoring of evapotranspiration using the SEBAL
1012 algorithm and Google Earth Engine cloud computing. *ISPRS Journal of Photogrammetry and*
1013 *Remote Sensing*, 178, 81–96. doi:10.1016/j.isprsjprs.2021.05.018
- 1014 Lhomme, J. P., Chehbouni, A., & Monteny, B. (2000). Sensible Heat Flux-Radiometric Surface
1015 Temperature Relationship Over Sparse Vegetation: Parameterizing B-1. *Boundary-Layer*
1016 *Meteorology*, 97(3), 431–457. doi:10.1023/a:1002786402695
- 1017 Liao, J. J., & Lewis, J. W. (2000). A note on concordance correlation coefficient. *PDA Journal of*
1018 *Pharmaceutical Science and Technology*, 54(1), 23-26.
- 1019 Lima, A. L. A., & Rodal, M. J. N. (2010). Phenology and wood density of plants growing in the semi-
1020 arid region of northeastern Brazil. *Journal of Arid Environments*, 74(11), 1363–1373.
1021 doi:10.1016/j.jaridenv.2010.05.009
- 1022 Lima, A. L. A., Sá Barretto Sampaio, E. V., Castro, C. C., Rodal, M. J. N., Antonino, A. C. D., & de
1023 Melo, A. L. (2012). Do the phenology and functional stem attributes of woody species allow for the
1024 identification of functional groups in the semiarid region of Brazil? *Trees*, 26(5), 1605–1616.
1025 doi:10.1007/s00468-012-0735-2
- 1026 Lima, C. E. S. de, Costa, V. S. de O., Galvíncio, J. D., Silva, R. M. da, & Santos, C. A. G. (2021).
1027 Assessment of automated evapotranspiration estimates obtained using the GP-SEBAL algorithm for

1028 dry forest vegetation (Caatinga) and agricultural areas in the Brazilian semiarid region. *Agricultural*
1029 *Water Management*, 250, 106863. doi:10.1016/j.agwat.2021.106863

1030 Lin, L. K. (1989). A concordance correlation coefficient to evaluate reproducibility. *Biometrics*, 45(1),
1031 255–268. <https://doi.org/10.2307/2532051>

1032 Liu, S., Lu, L., Mao, D., & Jia, L. (2007). Evaluating parameterizations of aerodynamic resistance to
1033 heat transfer using field measurements. *Hydrology and Earth System Sciences*, 11(2), 769–783.
1034 doi:10.5194/hess-11-769-2007

1035 Liu, Y., Guo, W., Huang, H., Ge, J., & Qiu, B. (2021). Estimating global aerodynamic parameters in
1036 1982–2017 using remote-sensing data and a turbulent transfer model. *Remote Sensing of*
1037 *Environment*, 260, 112428. doi:10.1016/j.rse.2021.112428

1038 Long, D., Gao, Y., & Singh, V. P. (2010). Estimation of daily average net radiation from MODIS data
1039 and DEM over the Baiyangdian watershed in North China for clear sky days. *Journal of Hydrology*,
1040 388(3–4), 217–233. doi:10.1016/j.jhydrol.2010.04.042

1041 Long, D., Singh, V. P., & Li, Z.-L. (2011). How sensitive is SEBAL to changes in input variables,
1042 domain size and satellite sensor? *Journal of Geophysical Research: Atmospheres*, 116(D21).
1043 Portico. doi:10.1029/2011jd016542

1044 Maia, V. A., de Souza, C. R., de Aguiar-Campos, N., Fagundes, N. C. A., Santos, A. B. M., de Paula,
1045 G. G. P., ... dos Santos, R. M. (2020). Interactions between climate and soil shape tree community
1046 assembly and above-ground woody biomass of tropical dry forests. *Forest Ecology and*
1047 *Management*, 474, 118348. doi:10.1016/j.foreco.2020.118348

1048 Mallick, K., Wandera, L., Bhattarai, N., Hostache, R., Kleniewska, M., & Chormanski, J. (2018). A
1049 critical evaluation on the role of aerodynamic and canopy–surface conductance parameterization in
1050 SEB and SVAT models for simulating evapotranspiration: A case study in the Upper Biebrza National
1051 Park Wetland in Poland. *Water*, 10(12), 1753. doi.org/10.3390/w10121753

1052 Marques, T. V., Mendes, K., Mutti, P., Medeiros, S., Silva, L., Perez-Marin, A. M., ... Bezerra, B.
1053 (2020). Environmental and biophysical controls of evapotranspiration from Seasonally Dry Tropical
1054 Forests (Caatinga) in the Brazilian Semiarid. *Agricultural and Forest Meteorology*, 287, 107957.
1055 doi:10.1016/j.agrformet.2020.107957

1056 McShane, R. R., Driscoll, K. P., & Sando, R. (2017). A review of surface energy balance models for
1057 estimating actual evapotranspiration with remote sensing at high spatiotemporal resolution over
1058 large extents. *Scientific Investigations Report*. doi:10.3133/sir20175087

1059 Medeiros, R., Andrade, J., Ramos, D., Moura, M., Pérez-Marin, A., dos Santos, C., ... Cunha, J.
1060 (2022). Remote Sensing Phenology of the Brazilian Caatinga and Its Environmental Drivers. *Remote*
1061 *Sensing*, 14(11), 2637. doi:10.3390/rs14112637

1062 Meier, R., Davin, E. L., Swenson, S. C., Lawrence, D. M., & Schwaab, J. (2019). Biomass heat
1063 storage dampens diurnal temperature variations in forests. *Environmental Research Letters*, 14(8),
1064 084026. doi:10.1088/1748-9326/ab2b4e

1065 Melo, D. C. D., Anache, J. A. A., Borges, V. P., Miralles, D. G., Martens, B., Fisher, J. B., ...
1066 Wendland, E. (2021). Are remote sensing evapotranspiration models reliable across South American
1067 ecoregions? *Water Resources Research*, 57(11). doi:10.1029/2020wr028752

1068 Mhaweji, M., Caiserman, A., Nasrallah, A., Dawi, A., Bachour, R., & Faour, G. (2020). Automated
1069 evapotranspiration retrieval model with missing soil-related datasets: The proposal of SEBALL.
1070 *Agricultural Water Management*, 229, 105938. doi:10.1016/j.agwat.2019.105938

1071 Miles, L., Newton, A. C., DeFries, R. S., Ravillious, C., May, I., Blyth, S., ... Gordon, J. E. (2006). A
1072 global overview of the conservation status of tropical dry forests. *Journal of Biogeography*, 33(3),
1073 491–505. doi:10.1111/j.1365-2699.2005.01424.x

1074 Miranda, R. Q., Nóbrega, R. L. B., Moura, M. S. B., Raghavan, S., & Galvíncio, J. D. (2020). Realistic
1075 and simplified models of plant and leaf area indices for a seasonally dry tropical forest. *International*

1076 Journal of Applied Earth Observation and Geoinformation, 85, 101992.
1077 doi:10.1016/j.jag.2019.101992

1078 Miranda, R. D. Q., Galvencio, J. D., Morais, Y. C. B., Moura, M. S. B. D., Jones, C. A., & Srinivasan,
1079 R. (2018). Dry forest deforestation dynamics in Brazil's Pontal Basin. *Revista Caatinga*, 31, 385-395.
1080 doi:10.1590/1983-21252018v31n215rc

1081 Mohan, M. M. P., Kanchirapuzha, R., & Varma, M. R. R. (2020a). Review of approaches for the
1082 estimation of sensible heat flux in remote sensing-based evapotranspiration models. *Journal of*
1083 *Applied Remote Sensing*, 14(04). doi:10.1117/1.jrs.14.041501

1084 Mohan, M. P.; Kanchirapuzha, R., & Varma, M. R. R. (2020b). Integration of soil moisture as an
1085 auxiliary parameter for the anchor pixel selection process in SEBAL using Landsat 8 and Sentinel-
1086 1A images. *International Journal of Remote Sensing*, 41(3), 1214-1231.

1087 Moro, M. F., Silva, I. A., Araújo, F. S. de, Nic Lughadha, E., Meagher, T. R., & Martins, F. R. (2015).
1088 The role of edaphic environment and climate in structuring phylogenetic pattern in Seasonally Dry
1089 Tropical Plant Communities. *PLOS ONE*, 10(3), e0119166. doi:10.1371/journal.pone.0119166

1090 Moro, M. F., Nic Lughadha, E., de Araújo, F. S., & Martins, F. R. (2016). A Phytogeographical
1091 Metaanalysis of the Semiarid Caatinga domain in Brazil. *The Botanical Review*, 82(2), 91–148.
1092 doi:10.1007/s12229-016-9164-z

1093 Mu, Q., Zhao, M., & Running, S. W. (2011). Improvements to a MODIS global terrestrial
1094 evapotranspiration algorithm. *Remote Sensing of Environment*, 115(8), 1781–1800.
1095 doi:10.1016/j.rse.2011.02.019

1096 Muñoz Sabater, J., (2019): ERA5-Land hourly data from 1981 to present. Copernicus Climate
1097 Change Service (C3S) Climate Data Store (CDS). (Accessed on 23-Feb-2022),
1098 doi:10.24381/cds.e2161bac

1099 Mutti, P. R., da Silva, L. L., Medeiros, S. de S., Dubreuil, V., Mendes, K. R., Marques, T. V., ...
1100 Bezerra, B. G. (2019). Basin scale rainfall-evapotranspiration dynamics in a tropical semiarid

1101 environment during dry and wet years. *International Journal of Applied Earth Observation and*
1102 *Geoinformation*, 75, 29–43. doi:10.1016/j.jag.2018.10.007

1103 Murray, T., and Verhoef, A. (2007) Moving towards a more mechanistic approach in the
1104 determination of soil heat flux from remote measurements. II. Diurnal shape of soil heat flux.
1105 *Agricultural and Forest Meteorology*, 147: 88-97.

1106 Nash, J. E., & Sutcliffe, J. V. (1970). River flow forecasting through conceptual models part I - A
1107 discussion of principles. *Journal of Hydrology*, 10(3), 282–290. doi:10.1016/0022-1694(70)90255-6

1108 Oliveira, M. L., Santos, C. A. C., Oliveira, G., Perez-Marin, A. M., & Santos, C. A. G. (2021). Effects
1109 of human-induced land degradation on water and carbon fluxes in two different Brazilian dryland soil
1110 covers. *Science of the Total Environment*, 792, 148458. doi:10.1016/j.scitotenv.2021.148458

1111 Owen, P. R., & Thomson, W. R. (1963). Heat transfer across rough surfaces. *Journal of Fluid*
1112 *Mechanics*, 15(3), 321–334. doi:10.1017/s0022112063000288

1113 Paloschi, R. A., Ramos, D. M., Ventura, D. J., Souza, R., Souza, E., Morellato, L. P. C., ... Borma,
1114 L. D. S. (2020). Environmental drivers of water use for Caatinga woody plant species: Combining
1115 remote sensing phenology and sap flow measurements. *Remote Sensing*, 13(1), 75.
1116 doi:10.3390/rs13010075

1117 Paul, G., Gowda, P. H., Vara Prasad, P. V., Howell, T. A., Staggenborg, S. A., & Neale, C. M. U.
1118 (2013). Lysimetric evaluation of SEBAL using high resolution airborne imagery from BEAREX08.
1119 *Advances in Water Resources*, 59, 157–168. doi:10.1016/j.advwatres.2013.06.003

1120 Paul, G., Gowda, P. H., Vara Prasad, P. V., Howell, T. A., Aiken, R. M., & Neale, C. M. U. (2014).
1121 Investigating the influence of roughness length for heat transport (zoh) on the performance of SEBAL
1122 in semi-arid irrigated and dryland agricultural systems. *Journal of Hydrology*, 509, 231–244.
1123 doi:10.1016/j.jhydrol.2013.11.040

- 1124 Paulson, C. A. (1970). The mathematical representation of wind speed and temperature profiles in
1125 the unstable atmospheric surface layer. *Journal of Applied Meteorology and Climatology*, 9(6), 857-
1126 861. doi:10.1175/1520-0450(1970)009%3C0857:tmrows%3E2.0.co;2
- 1127 Pennington, R. T., Lewis, G. P., & Ratter, J. A. (Eds.). (2006). An overview of the plant diversity,
1128 biogeography and conservation of Neotropical Savannas and Seasonally Dry Forests. *Neotropical*
1129 *Savannas and Seasonally Dry Forests*, 1–29. doi:10.1201/9781420004496-1
- 1130 Pennington, R. T., Lavin, M., & Oliveira-Filho, A. (2009). Woody plant diversity, evolution, and
1131 ecology in the Tropics: Perspectives from Seasonally Dry Tropical Forests. *Annual Review of*
1132 *Ecology, Evolution, and Systematics*, 40(1), 437–457. doi:10.1146/annurev.ecolsys.110308.120327
- 1133 Pennington, R. T., Lehmann, C. E. R., & Rowland, L. M. (2018). Tropical savannas and dry forests.
1134 *Current Biology*, 28(9), R541–R545. doi:10.1016/j.cub.2018.03.014
- 1135 Potapov, P., Li, X., Hernandez-Serna, A., Tyukavina, A., Hansen, M. C., Kommareddy, A., ... Hofton,
1136 M. (2021). Mapping global forest canopy height through integration of GEDI and Landsat data.
1137 *Remote Sensing of Environment*, 253, 112165. doi:10.1016/j.rse.2020.112165
- 1138 Priestley, C. H. B., & Taylor, R. J. (1972). On the assessment of surface heat flux and evaporation
1139 using large-scale parameters. *Monthly Weather Review*, 100(2), 81–92. doi:10.1175/1520-
1140 0493(1972)100<0081:otaosh>2.3.co;2
- 1141 Queiroz, L. P., Cardoso, D., Fernandes, M. F., & Moro, M. F. (2017). Diversity and evolution of
1142 flowering plants of the Caatinga domain. *Caatinga*, 23–63. doi:10.1007/978-3-319-68339-3_2
- 1143 Queiroz, M. G. D., Silva, T. G. F. D., Souza, C. A. A. D., Jardim, A. M. D. R. F., Araújo Júnior, G. D.
1144 N., Souza, L. S. B. D., & Moura, M. S. B. D. (2020). Composition of Caatinga species under anthropic
1145 disturbance and its correlation with rainfall partitioning. *Floresta e Ambiente*, 28. doi:10.1590/2179-
1146 8087-FLORAM-2019-0044

1147 Ramoelo, A., Majozi, N., Mathieu, R., Jovanovic, N., Nickless, A., & Dzikiti, S. (2014). Validation of
1148 global evapotranspiration product (MOD16) using flux tower data in the African Savanna, South
1149 Africa. *Remote Sensing*, 6(8), 7406–7423. doi:10.3390/rs6087406

1150 Rasp, S., Pritchard, M. S., & Gentine, P. (2018). Deep learning to represent subgrid processes in
1151 climate models. *Proceedings of the National Academy of Sciences*, 115(39), 9684–9689.
1152 doi:10.1073/pnas.1810286115

1153 Raupach, M. R. (1992). Drag and drag partition on rough surfaces. *Boundary-Layer Meteorology*,
1154 60(4), 375–395. doi.org/10.1007/bf00155203

1155 Raupach, M. R. (1994). Simplified expressions for vegetation roughness length and zero-plane
1156 displacement as functions of canopy height and area index. *Boundary-Layer Meteorology*, 71(1–2),
1157 211–216. doi:10.1007/bf00709229

1158 Roberts, W., Williams, G. P., Jackson, E., Nelson, E. J., & Ames, D. P. (2018). Hydrostats: A Python
1159 package for characterizing errors between observed and predicted time series. *Hydrology*, 5(4), 66.
1160 doi:10.3390/hydrology5040066

1161 Rodell, M., Houser, P. R., Jambor, U., Gottschalck, J., Mitchell, K., Meng, C.-J., ... Toll, D. (2004).
1162 The Global Land Data Assimilation System. *Bulletin of the American Meteorological Society*, 85(3),
1163 381–394. doi:10.1175/bams-85-3-381

1164 Running, S., Mu, Q., Zhao, M. (2017). MOD16A2 MODIS/Terra Net Evapotranspiration 8-Day L4
1165 Global 500m SIN Grid V006 [Data set]. NASA EOSDIS Land Processes DAAC. Accessed 23-Feb-
1166 2022 from doi:10.5067/MODIS/MOD16A2.006

1167 Sahnoun, F., Abderrahmane, H., Kaddour, M., Abdelkader, K., Mohamed, B., & Castro, T. A. H. D.
1168 (2021). Application of SEBAL and T s/VI trapezoid models for estimating actual evapotranspiration
1169 in the Algerian Semi-Arid Environment to improve agricultural water management. *Revista Brasileira
1170 de Meteorologia*, 36, 219-236. doi:10.1590/0102-77863610020

1171 Salazar-Martínez, D., Holwerda, F., Holmes, T. R. H., Yépez, E. A., Hain, C. R., Alvarado-Barrientos,
1172 S., ... Vivoni, E. R. (2022). Evaluation of remote sensing-based evapotranspiration products at low-
1173 latitude eddy covariance sites. *Journal of Hydrology*, 610, 127786.
1174 doi:10.1016/j.jhydrol.2022.127786

1175 Santos, R. M., Oliveira-Filho, A. T., Eisenlohr, P. V., Queiroz, L. P., Cardoso, D. B. O. S., & Rodal,
1176 M. J. N. (2012). Identity and relationships of the Arboreal Caatinga among other floristic units of
1177 seasonally dry tropical forests (SDTFs) of north-eastern and Central Brazil. *Ecology and Evolution*,
1178 2(2), 409–428. doi:10.1002/ece3.91

1179 Santos, M. G., Oliveira, M. T., Figueiredo, K. V., Falcão, H. M., Arruda, E. C. P., Almeida-Cortez, J.,
1180 ... Antonino, A. C. D. (2014). Caatinga, the Brazilian dry tropical forest: can it tolerate climate
1181 changes? *Theoretical and Experimental Plant Physiology*, 26(1), 83–99. doi:10.1007/s40626-014-
1182 0008-0

1183 Santos, C. A. C., Mariano, D. A., das Chagas A. do Nascimento, F., da C. Dantas, F. R., de Oliveira,
1184 G., Silva, M. T., ... Neale, C. M. U. (2020). Spatio-temporal patterns of energy exchange and
1185 evapotranspiration during an intense drought for drylands in Brazil. *International Journal of Applied*
1186 *Earth Observation and Geoinformation*, 85, 101982. doi:10.1016/j.jag.2019.101982

1187 Schaaf, C., & Wang, Z. (2015). MCD43A4 MODIS/Terra+Aqua BRDF/Albedo Nadir BRDF Adjusted
1188 Ref Daily L3 Global - 500m V006 [Data set]. NASA EOSDIS Land Processes DAAC. Accessed 23-
1189 Feb-2022. doi:10.5067/MODIS/MCD43A4.006

1190 Senay, G. B., Bohms, S., Singh, R. K., Gowda, P. H., Velpuri, N. M., Alemu, H., & Verdin, J. P.
1191 (2013). Operational evapotranspiration mapping using remote sensing and weather datasets: A new
1192 parameterization for the SSEB approach. *JAWRA Journal of the American Water Resources*
1193 *Association*, 49(3), 577–591. Portico. <https://doi.org/10.1111/jawr.12057>

1194 Senay, G. B., Friedrichs, M., Morton, C., Parrish, G. E., Schauer, M., Khand, K., ... & Huntington, J.
1195 (2022). Mapping actual evapotranspiration using Landsat for the conterminous United States:

1196 Google Earth Engine implementation and assessment of the SSEBop model. *Remote Sensing of*
1197 *Environment*, 275, 113011. doi:10.1016/j.rse.2022.113011

1198 Senkondo, W., Munishi, S. E., Tumbo, M., Nobert, J., & Lyon, S. W. (2019). Comparing remotely-
1199 sensed surface energy balance evapotranspiration estimates in heterogeneous and data-limited
1200 regions: a case study of Tanzania's Kilombero Valley. *Remote Sensing*, 11(11), 1289.
1201 doi:10.3390/rs11111289

1202 Shuttleworth, W. J. (2012). *Terrestrial hydrometeorology*. John Wiley & Sons.

1203 Silva, A. M., da Silva, R. M., & Santos, C. A. G. (2019). Automated surface energy balance algorithm
1204 for land (ASEBAL) based on automating endmember pixel selection for evapotranspiration
1205 calculation in MODIS orbital images. *International Journal of Applied Earth Observation and*
1206 *Geoinformation*, 79, 1–11. doi:10.1016/j.jag.2019.02.012

1207 Silva, J. M. C.; LEAL, I.R.; Tabarelli, M. (Ed.). (2017a). *Caatinga: the largest tropical dry forest region*
1208 *in South America*. Springer.

1209 Silva, P. F. da, Lima, J. R. de S., Antonino, A. C. D., Souza, R., Souza, E. S. de, Silva, J. R. I., &
1210 Alves, E. M. (2017b). Seasonal patterns of carbon dioxide, water and energy fluxes over the
1211 Caatinga and grassland in the semi-arid region of Brazil. *Journal of Arid Environments*, 147, 71–82.
1212 doi:10.1016/j.jaridenv.2017.09.003

1213 Singh, R. K., & Irmak, A. (2011). Treatment of anchor pixels in the METRIC model for improved
1214 estimation of sensible and latent heat fluxes. *Hydrological Sciences Journal*, 56(5), 895–906.
1215 doi:10.1080/02626667.2011.587424

1216 Singh, R. K., Liu, S., Tieszen, L. L., Suyker, A. E., & Verma, S. B. (2012). Estimating seasonal
1217 evapotranspiration from temporal satellite images. *Irrigation Science*, 30(4), 303-313.
1218 doi:10.1007/s00271-011-0287-z

- 1219 Souza, L. S. B. de, Moura, M. S. B. de, Sedyama, G. C., & Silva, T. G. F. da. (2015). Balanço de
1220 energia e controle biofísico da evapotranspiração na Caatinga em condições de seca intensa.
1221 Pesquisa Agropecuária Brasileira, 50(8), 627–636. doi:10.1590/s0100-204x2015000800001
- 1222 Stewart, J. B., Kustas, W. P., Humes, K. S., Nichols, W. D., Moran, M. S., & de Bruin, H. A. (1994).
1223 Sensible heat flux-radiometric surface temperature relationship for eight semiarid areas. Journal of
1224 Applied Meteorology and Climatology, 33(9), 1110-1117. doi:10.1175/1520-
1225 0450(1994)033%3C1110:shfrst%3E2.0.co;2
- 1226 Su, Z., Schmugge, T., Kustas, W. P., & Massman, W. J. (2001). An evaluation of two models for
1227 estimation of the roughness height for heat transfer between the land surface and the atmosphere.
1228 Journal of Applied Meteorology, 40(11), 1933-1951. doi:10.1175/1520-
1229 0450(2001)040%3C1933:aeotmf%3E2.0.co;2
- 1230 Su, Z. (2002). The Surface Energy Balance System (SEBS) for estimation of turbulent heat fluxes.
1231 Hydrology and Earth System Sciences, 6(1), 85–100. doi:10.5194/hess-6-85-2002
- 1232 Swenson, S. C., Burns, S. P., & Lawrence, D. M. (2019). The Impact of Biomass Heat Storage on
1233 the Canopy Energy Balance and Atmospheric Stability in the Community Land Model. Journal of
1234 Advances in Modeling Earth Systems, 11(1), 83–98. Portico. doi:10.1029/2018ms001476
- 1235 Teixeira, A. D. C., Bastiaanssen, W. G., Ahmad, M., & Bos, M. G. (2009). Reviewing SEBAL input
1236 parameters for assessing evapotranspiration and water productivity for the Low-Middle Sao
1237 Francisco River basin, Brazil: Part A: Calibration and validation. Agricultural and Forest Meteorology,
1238 149(3-4), 462-476. doi:10.1016/j.agrformet.2008.09.016
- 1239 Thom, A. S. (1972). Momentum, mass and heat exchange of vegetation. Quarterly Journal of the
1240 Royal Meteorological Society, 98(415), 124–134. doi:10.1002/qj.49709841510
- 1241 Tomasella, J., Silva Pinto Vieira, R. M., Barbosa, A. A., Rodriguez, D. A., Oliveira Santana, M. de, &
1242 Sestini, M. F. (2018). Desertification trends in the Northeast of Brazil over the period 2000–2016.

- 1243 International Journal of Applied Earth Observation and Geoinformation, 73, 197–206.
1244 doi:10.1016/j.jag.2018.06.012
- 1245 Trebs, I., Mallick, K., Bhattarai, N., Sulis, M., Cleverly, J., Woodgate, W., Silberstein, R., Hinko-
1246 Najera, N., Beringer, J., Meyer, W. S., Su, Z., & Boulet, G. (2021). The role of aerodynamic
1247 resistance in thermal remote sensing-based evapotranspiration models. EGU General Assembly.
1248 doi.org/10.5194/egusphere-egu21-2186Remote Sensing of Environment, 264, 112602.
1249 doi:10.1016/j.rse.2021.112602
- 1250 Trezza, R. (2006). Evapotranspiration from a remote sensing model for water management in an
1251 irrigation system in Venezuela. *Interciencia*, 31(6), 417-423
- 1252 Trezza, R., Allen, R., & Tasumi, M. (2013). Estimation of Actual Evapotranspiration along the Middle
1253 Rio Grande of New Mexico Using MODIS and Landsat Imagery with the METRIC Model. *Remote*
1254 *Sensing*, 5(10), 5397–5423. doi:10.3390/rs5105397
- 1255 Troufleau, D., Lhomme, J. P., Monteny, B., & Vidal, A. (1997). Sensible heat flux and radiometric
1256 surface temperature over sparse Sahelian vegetation. I. An experimental analysis of the kB–1
1257 parameter. *Journal of Hydrology*, 188, 815-838. doi:10.1016/s0022-1694(96)03172-1
- 1258 Verhoef, A., De Bruin, H. A. R., & Van Den Hurk, B. J. J. M. (1997a). Some practical notes on the
1259 parameter kB–1 for sparse vegetation. *Journal of Applied Meteorology*, 36(5), 560-572.
1260 doi:10.1175/1520-0450(1997)036%3C0560:spnotp%3E2.0.co;2
- 1261 Verhoef, A., McNaughton, K. G., & Jacobs, A. F. G. (1997b). A parameterization of momentum
1262 roughness length and displacement height for a wide range of canopy densities. *Hydrology and Earth*
1263 *System Sciences*, 1(1), 81–91. doi:10.5194/hess-1-81-1997
- 1264 Wang, C., Yang, J., Myint, S. W., Wang, Z.-H., & Tong, B. (2016). Empirical modeling and spatio-
1265 temporal patterns of urban evapotranspiration for the Phoenix metropolitan area, Arizona. *GIScience*
1266 *& Remote Sensing*, 53(6), 778–792. doi:10.1080/15481603.2016.1243399

- 1267 Wilson, K., Goldstein, A., Falge, E., Aubinet, M., Baldocchi, D., Berbigier, P., ... Verma, S. (2002).
1268 Energy balance closure at FLUXNET sites. *Agricultural and Forest Meteorology*, 113(1-4), 223–243.
1269 doi:10.1016/s0168-1923(02)00109-0
- 1270 WRB, I.W.G., 2006. World reference base for soil resources 2006, 2nd ed. In: FAO (ed.), *World Soil*
1271 *Resources Reports No. 103*, Rome. ISBN 92-5-105511-4.
- 1272 Wu, Q. (2020). geemap: A Python package for interactive mapping with Google Earth Engine.
1273 *Journal of Open Source Software*, 5(51), 2305. doi:10.21105/joss.02305
- 1274 Yin, L., Wang, X., Feng, X., Fu, B., & Chen, Y. (2020). A comparison of SSEBop-Model-Based
1275 evapotranspiration with eight evapotranspiration products in the Yellow River Basin, China. *Remote*
1276 *Sensing*, 12(16), 2528. doi:10.3390/rs12162528
- 1277 Zhang, Y., Kong, D., Gan, R., Chiew, F. H. S., McVicar, T. R., Zhang, Q., & Yang, Y. (2019). Coupled
1278 estimation of 500 m and 8-day resolution global evapotranspiration and gross primary production in
1279 2002–2017. *Remote Sensing of Environment*, 222, 165–182. doi:10.1016/j.rse.2018.12.031
- 1280 Zhao, M., Heinsch, F. A., Nemani, R. R., & Running, S. W. (2005). Improvements of the MODIS
1281 terrestrial gross and net primary production global data set. *Remote sensing of Environment*, 95(2),
1282 164-176. doi:10.1016/j.rse.2004.12.011